USGS
science for a changing world

The M_W 6.0 South Napa Earthquake of August 24, 2014—Observations of Surface Faulting and Ground Deformation, with Recommendations for Improving Post-Earthquake Field Investigations

By Daniel J. Ponti, Carla M. Rosa, and James Luke Blair

Open-File Report 2019–1018

U.S. Department of the Interior
U.S. Geological Survey

U.S. Department of the Interior
DAVID BERNHARDT, Acting Secretary

U.S. Geological Survey
James F. Reilly II, Director

U.S. Geological Survey, Reston, Virginia: 2019

Suggested citation:
Ponti, D.J, Rosa, C.M, and Blair, J.L., 2019, The M_w 6.0 South Napa earthquake of August 24, 2014—Observations of surface faulting and ground deformation, with recommendations for improving post-earthquake field investigations: U.S. Geological Survey Open-File Report 2019–1018, 50 p., 15 appendixes, https://doi.org/10.3133/ofr20191018.

ISSN 2331-1258 (online)

Contributors

U.S. Geological Survey
Benjamin A. Brooks
Emma Crewdson
Coyn Criley
Stephen B. DeLong
Suzanne Hecker
Thomas L. Holzer
Kenneth W. Hudnut
James J. Lienkaemper
Alexandra J. Pickering
Daniel J. Ponti
Carol S. Prentice
Carla M. Rosa
David P. Schwartz
Robert R. Sickler
John C. Tinsley III
California Geological Survey
Clif Davenport
Timothy E. Dawson
Marc P. Delattre
Wayne Haydon
Jeremy Lancaster
Maxime Mareschal
Cynthia Pridmore
Ron S. Rubin
Gordon G. Seitz
Mark O. Wiegers
Chris Wills
Fugro
Cooper Brossy
Michael Buga
David Trench
California Department of Water Resources
Don Hoirup
Infraterra
Chris Hitchcock
Andy Lutz
U.S. Army Corps of Engineers
Keith Kelson
University of California, Davis
Alex Morelan
Chad Trexler
RGH Consultants
Jared Pratt
Ryan Geological Consulting
Kevin Ryan
AMEC
Donald Wells
Office of Mine Reclamation
John Wesling
Unaffiliated
Heidi Stenner
Dana Zaccone

Contents

Figures

Tables

Conversion Factors

U.S. customary units to International System of Units

Multiply	By	To obtain
	Length	
inch (in.)	2.54	centimeter (cm)
inch (in.)	25.4	millimeter (mm)
foot (ft)	0.3048	meter (m)
mile (mi)	1.609	kilometer (km)
mile, nautical (nmi)	1.852	kilometer (km)
yard (yd)	0.9144	meter (m)

International System of Units to U.S. customary units

Multiply	By	To obtain
	Length	
centimeter (cm)	0.3937	inch (in.)
millimeter (mm)	0.03937	inch (in.)
meter (m)	3.281	foot (ft)
kilometer (km)	0.6214	mile (mi)
kilometer (km)	0.5400	mile, nautical (nmi)
meter (m)	1.094	yard (yd)

Datum

Vertical coordinate information is referenced to the North American Vertical Datum of 1988 (NAVD 88).
Horizontal coordinate information is referenced to the World Geodetic System 1984 datum (WGS84).

The M_w 6.0 South Napa Earthquake of August 24, 2014—Observations of Surface Faulting and Ground Deformation, with Recommendations for Improving Post-Earthquake Field Investigations

By Daniel J. Ponti,[1] Carla M. Rosa,[2] and James Luke Blair[1]

Abstract

The M_w 6.0 South Napa earthquake of August 24, 2014, produced complex and extensive surface faulting and other ground deformation features. Following the event, geologists made more than 1,200 field observations at locations where tectonic faulting and ground failure produced visible deformation that fractured and disturbed the ground surface. At a few locations, large-scale, detailed, field-based maps of fault rupture and ground deformation were produced. The South Napa earthquake response was one of the first times when post-earthquake reconnaissance data were mostly collected and disseminated electronically. The advantages and opportunities these new methods bring to our research also pose new challenges to large-scale compilation efforts and demonstrate the value of developing guidelines and better standardization across the community to more optimally utilize developing technology in future post-earthquake investigations. Some suggestions for standardizing the collection and dissemination of post-earthquake field reconnaissance data are provided herein.

Field observations and maps were integrated with airborne imagery, lidar, and InSAR to produce a comprehensive, large-scale digital map of fault rupture and zones of ground deformation. The map, observations, and photo database are summarized here in appendixes and figures and are also available as a series of digital data products within a companion U.S. Geological Survey data release (Ponti and others, 2019); the characteristics of fault rupture and ground deformation features are summarized in detail in the body of this report.

The results of this compilation reveal that faulting occurred within a 2-km-wide zone on six, roughly parallel traces within the West Napa Fault System. Most of the fault slip, and all the afterslip, occurred on the 21-km-long westernmost trace (Trace A). Maximum coseismic slip was greater than 40 cm and possibly as great as 60 cm, with the slip maximum located about 10 km north of the epicenter. Extensive ground deformation also occurred off the principal fault traces. Deformation characteristics of these features were not consistent with either primary faulting or shaking-induced ground failure and remain enigmatic, although this report includes speculation about possible origins.

[1]U.S. Geological Survey
[2]California Geological Survey

The use of InSAR was invaluable for identifying and mapping secondary traces with small displacements, and for delineating the overall details of the extensive rupture. InSAR data also highlighted other areas with possible ground deformation—some of which are found coincident with previously mapped fault traces, whereas others are in areas where no faults were previously mapped. Several of these regions had no visible ground deformation, whereas others did produce features that were inconsistent with tectonic faulting, so care must be taken not to over interpret the InSAR data without careful, corroborating field investigations.

Introduction

The M_w 6.0 South Napa earthquake occurred on Sunday, August 24, 2014, in Napa County, California and produced substantial surface fault rupture distributed along several traces of the West Napa Fault System (Hudnut and others, 2014; Brocher and others, 2015; DeLong and others, 2016) along with other ground deformation (fig. 1). The rupture nucleated at a depth of about 8.8 km (Brocher and others, 2015; Hardebeck and Shelley, 2016) with the hypocenter directly beneath the Napa River about 3 km southwest of the Napa County Airport and about 10 km south-southwest of downtown Napa (fig. 1). The West Napa Fault System is generally considered to be a minor contributor to fault slip and earthquake hazard within the approximately 100-km-wide San Andreas Fault System, with an estimated slip rate of less than 2 mm/year and average rate of recurrence for $M \geq 6.7$ events greater than 1,000 years (Field and others, 2014), although there are few actual constraints on the West Napa Fault System's earthquake behavior, and no fault-specific geologic estimates of earthquake recurrence, fault slip rate, or maximum earthquake magnitude (Hudnut and others, 2014).

Besides being the largest earthquake to strike the San Francisco Bay area since the 1989 M_w 6.9 Loma Prieta earthquake, the 2014 South Napa earthquake is notable in that the surface fault rupture is quite widespread for an earthquake of M_w 6.0 (fig. 1). The South Napa earthquake has produced the longest coseismic surface rupture and the largest coseismic surficial displacement when compared to 11 strike-slip earthquakes with similar magnitudes that have occurred in California since 1948 (Brocher and others, 2015; Hudnut and others, 2014). Furthermore, surface rupture involved tectonic slip on at least six distinct fault traces distributed across a 2-km-wide zone (fig. 1), whereas most other similar-sized earthquakes in California appeared to have involved surface slip on only one fault trace or no surface slip at all (Hudnut and others, 2014). The South Napa earthquake is also notable for the amount of postseismic creep (afterslip) that occurred along the principal trace (Trace A) (Lienkaemper and others, 2016). Afterslip and total slip across the fault zone(s) over longer apertures have been quantified and characterized by alignment arrays and both terrestrial and mobile lidar scans (Brooks and others, 2015; DeLong and others, 2016; Lienkaemper and others, 2016).

Because of its unique character among other similar-sized events, and location within the densely populated San s Bay area, the South Napa earthquake surface rupture is being studied in detail using a wide range of methods to better characterize the nature of the West Napa Fault System and its seismic hazard potential. Fundamental to these analyses is the initial documentation of surface faulting and ground deformation from direct field observations made shortly after the event. In the weeks following the South Napa earthquake, geologists from the U.S. Geological Survey (USGS); California Geological Survey (CGS); and University of California, Davis (UCD) and several consulting geologists made more than 1,200 field observations and took photographs at more than 1,000 locations where ground deformation fractured and disturbed soil, buildings, roadways, and other infrastructure. Measurements of fault

slip and ground displacement were obtained in the field at more than 270 sites. In addition to site-specific observations, detailed maps of fault rupture and ground deformation were also produced for select locations. Coordination in the field was supported by the California Earthquake Clearinghouse, whose partners include CGS, USGS, the Earthquake Engineering Research Institute (EERI), and the California Office of Emergency Services (CalOES) through the opening of a physical clearinghouse in Napa where geologists could meet to share observations and plan future efforts (Rosinski and others, 2015). The Clearinghouse was instrumental in supporting the ground reconnaissance effort through coordinating acquisition of remote sensing products (Hudnut and others, 2014; Rosinski and others, 2015), which were also used for compiling the fault rupture data. High-resolution, orthorectified, post-earthquake airborne imagery; post-earthquake airborne lidar; and interferometric synthetic aperture radar (InSAR) became available soon after the event. Given how widespread the South Napa earthquake surface rupture is, these resources were invaluable in directing field crews to document ground rupture in areas outside of the principal fault rupture, and to verify continuity of rupture in inaccessible areas.

This report and companion data release (Ponti and others, 2019) present a comprehensive documentation of post-earthquake field investigations, including site-specific field descriptions, displacement measurements, photographs of surface rupture and ground deformation, and field-based maps of surface rupture in localized areas. These data are integrated with airborne imagery, lidar data, and InSAR data to produce a large-scale digital map of all known areas of ground deformation produced by the South Napa earthquake.

The South Napa earthquake response represents one of the first times when reconnaissance data was mainly collected and disseminated electronically. Although largely agricultural, the Napa Valley is heavily populated and has widespread cellular data coverage, which allowed field crews and office staff to communicate, share, and compile data readily, markedly improving the coordination between field and office staff (Morelan and others, 2015). Use of digital tablets, smart phones, and digital cameras, most with embedded Global Positioning System (GPS) devices, was widespread. Many investigators took advantage of mobile mapping and note-taking software programs that use digital forms, voice recognition, and other tools to speed data entry. Mobile communications, text messaging, and the use of online wikis and social media enabled effective coordination of field crews and rapid dissemination of information (Morelan and others, 2015). Thus, the amount of observational data collected and distributed is immense, and given that data can now be automatically georeferenced, field geologists no longer need to spend time transcribing and collating their information before disseminating it.

However, these advantages and opportunities pose new challenges to large-scale compilation efforts. Geographic data automatically recorded using devices such as smart phones and tablets vary in their precision and can be highly inaccurate. In addition, data collection methods vary among investigators, and there is no accepted standardized schema or format for collecting and transferring post-earthquake data, which poses compilation challenges. Furthermore, because data need not be reviewed before being disseminated, inevitable input errors are often not caught by the people collecting the data at a time when errors could have been more readily corrected. The South Napa earthquake response effort highlights the value of developing guidelines and greater standardization across the community to more optimally utilize developing technology in future post-earthquake investigations.

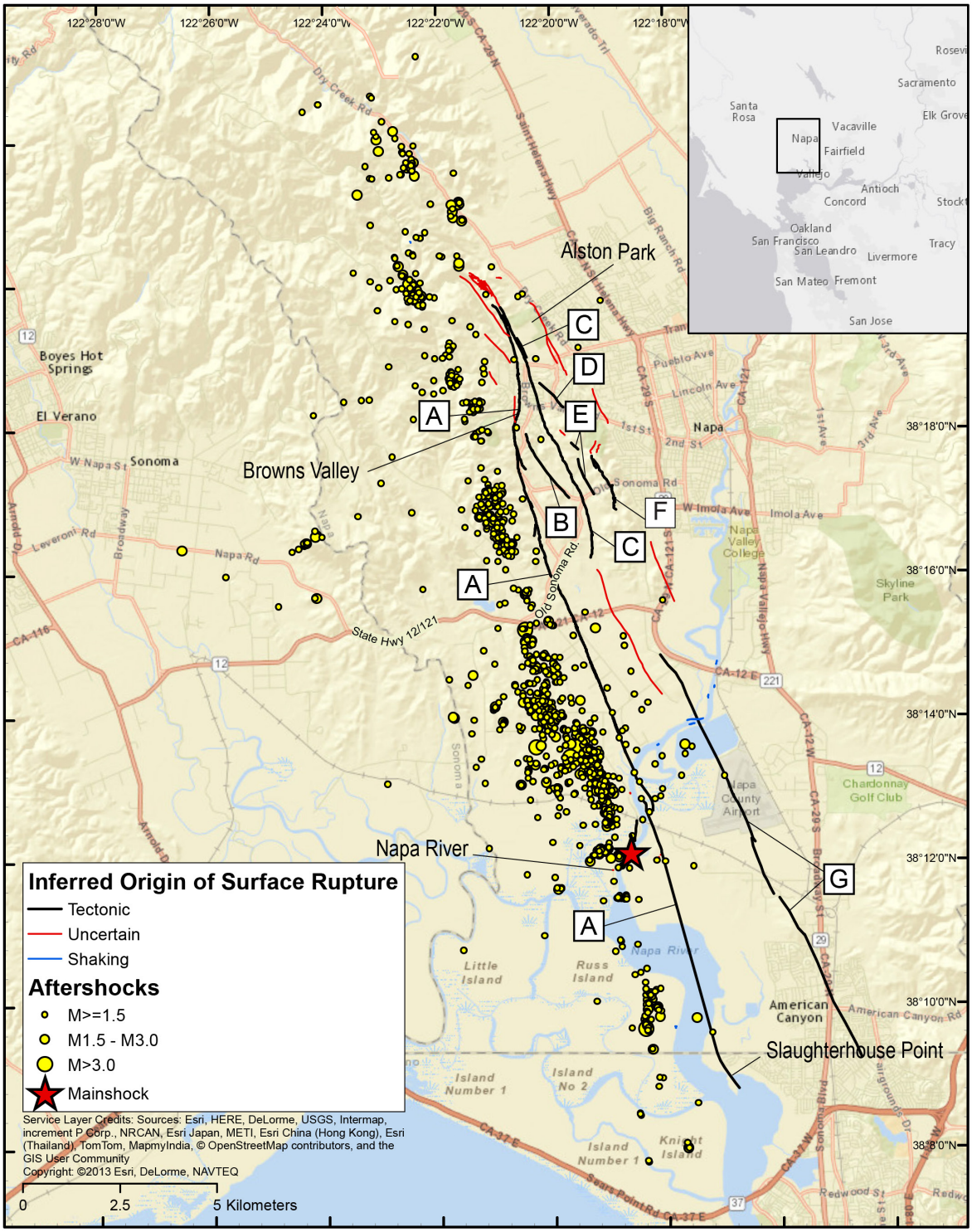

Figure 1. Map of surface faulting and ground deformation produced by the August 24, 2014, South Napa earthquake, locations of the mainshock and aftershocks that occurred between August 24 and November 4, 2014 (Hardebeck and Shelley, 2016), and locations referenced in the text. A–G show principal tectonic fault traces. Inset shows location of map area relative to San Francisco (located ~50 km south) and other major northern California cities.

Data Compilation

The appendixes and companion data release include observations submitted directly from field participants to USGS or CGS scientists or via the California Earthquake Clearinghouse (limited to observations of surface faulting and other ground deformation). All post-earthquake ground rupture observations and slip/displacement measurements are those in the public domain, including data that have been published in summary reports elsewhere (Brocher and others, 2015; Dawson and others, 2014; Morelan and others, 2015).

Observations of damage to buildings or earthen structures such as embankments or fills are included only insofar as they reflect deformation of the ground surface. Not included in this compilation are detailed observations of impacts to buildings or infrastructure that have been published elsewhere (Cohen-Waeber and others, 2014; Beyzaei and others, 2014; Harder, 2014; Wagner and others, 2014).

Site Observations

Overview

Most of the data collected and reported consist of notes, measurements, and photographs documenting the existence and character of ground deformation at a specific locality or site, with the location represented as a geographic point (defined by a latitude and longitude coordinate pair)[3]. Observations of ground deformation from the South Napa earthquake were documented at different levels of detail, which required standardization and reconciliation among different source datasets.

Investigators used a variety of methods to record site observations in the field. A notable aspect of the South Napa earthquake response is that many opted to use mobile technology to record observations directly, taking advantage of note-taking and mapping software on smartphones and mobile tablets to automatically geocode locations, tag observations to photographs, record and translate notes, and output information.

Regardless of their chosen methodology, geologists reported information in a variety of digital formats: for example, spreadsheet tables, GPS tracklogs, reports in pdf format, photographs or scanned drawings in various image file formats, text documents (email, text, or word processing files), Esri shapefiles, and KML/KMZ files. In addition to the different data formats, the recorded information was organized or classified in different ways depending on the observers' standards of practice. Overall, however, all information received from site observations falls into one or more of these categories:

- *Waypoints*.—Point data attributed only as to the presence or absence of faulting or ground deformation
- *GPS track logs*.—Points along traverses showing areas canvassed on the ground
- *Text descriptions*.—Descriptions of ground rupture referenced to a locality
- *Digital photographs*.—Photographs of ground rupture features, with or without embedded coordinate information or other camera metadata

[3]Data collected that did not include coordinate information were excluded from our compilation. This was also the case for analog or digital photographs that could not be readily geocoded against a GPS tracklog.

- *Measurements.*—Fault slip and fracture offset data; information may be tabulated into a spreadsheet or other type of table, or recorded in a text description

Waypoints and track logs were used to compile the rupture map but these data are not included in our compilation of field observations, except as noted below. The remaining types of data were combined into three data tables, named as follows: (1) Observations, which includes descriptions of ground rupture and displacement measurements; (2) No Deformation Observed, which includes locations along fault trends and InSAR lineaments where surface faulting was anticipated but where no evidence of ground disturbance was observed; and (3) Photos, which includes photo metadata with links to the associated digital images, and which are stored online and are part of the companion data release (Ponti and others, 2019). Many of the table attributes and photographs are included in the appendixes to this report. The companion data release (Ponti and others, 2019) includes full table data as tab-delimited text files (suitable for importing into GIS applications or spreadsheets) and summary observation and photo data in kmz format for viewing in Earth viewers such as Google Earth.

Each record in our Observations and No Deformation Observed tables constitutes a station, which is a location where an observation (text description, photograph, and [or] measurement) was made by a single investigator or a field team working together (an observer) during a single visit on a specific date. If the same observer revisits the same locality on a different day or time and records a separate observation, this constitutes a separate station in the Observations table. Minimum data recorded for a station in the Observations table are name(s) of the observer(s); observation date; locality coordinate (for example, latitude and longitude); and at least one of the following: (1) text describing the character of ground deformation, (2) measurement of slip or indication of displacement sense, or (3) one or more photographs.

In addition to recording information directly reported by field investigators, the Observations table contains several attributes that were derived during compilation; these include a classification of the type of feature or material affected by ground deformation and the interpreted origin of deformation inferred directly from the observation itself or from context, based on location and information from nearby stations. Definitions of the Observations and No Deformation Observed table attributes are given in table 1.

Table 1. Attribute definitions for the Observations and No Deformation Observed tables.

[Attribute names in bold are non-null fields]

Attribute	Data Type	Controlled Values	Definition
stnid	Integer		Identifier for the station. A station is assigned where descriptions, displacement measurements and (or) photographs have been obtained at a site at a given date and time by an observer or group of observers working together. Repeat observations at different times by the same observer or group of observers are assigned different stnids.
intid	Integer		Internal identifier. Used to link an observation record to associated records in the Photos table.
citation	Text		If the data or photographs from this observation are published elsewhere, the original publication is cited here.

Attribute	Data Type	Controlled Values	Definition
obs_date	Text		Date of the observation as year, numerical month, and day of month, each separated by colon (for example, 2014:09:03 represents September 3, 2014).
latitude	Float		Coordinates of the station in decimal degrees, WGS84 datum. These values are derived either from the coordinate provided directly by the observer, or are digitized during compilation using airborne imagery and ground photographs to more accurately locate the station on the feature of interest. Observations of fault features were typically relocated to coincide with mapped fault locations as derived from high-resolution imagery, lidar data, or InSAR data.
longitude	Float		
orig_lat	Float		Original latitude reported by the observer in decimal degrees, WGS84 datum.
orig_lon	Float		Original longitude reported by the observer in decimal degrees, WGS84 datum.
photo[1]	Text	Y or N	Y (Yes) or N (No) if photographs are associated with this station.
observer	Text		Last name of the observer or observers who provided the information/photographs. Full names and affiliations are listed on the report title page. A single name may be listed where observations may have been collected by a group of individuals working together.
observed_feature[1]	Text		The type of feature where fault offset is observed or the type of materials that are offset or disturbed.
		Curb/Sidewalk	Offset or damage to sidewalks and curbs located adjacent to roadways and constructed of concrete, although a small number of curbs may be of asphalt construction. This classification also includes concrete patios and pathways.
		Foundation	Offset or damage noted in concrete, brick/masonry, or wood perimeter foundations of structures.
		Pavement	Offset or damage to paved roadway and runway surfaces, dominantly made of bituminous asphalt or concrete. Includes gravel shoulders adjacent to paved roadways.
		Soil	Offset or fractures in soil and shallow fill. Includes compacted soil (such as dirt roads or trails) and gravel or mixed gravel/dirt roadways.
		Vineyard Row	Offset noted of a row or rows of grape vines and (or) stakes.
		Wall/Fence	Offset or disturbance noted in a vertical wall or fence constructed of wood, concrete or masonry.
		Other	Damage or offset from ground deformation to miscellaneous features not otherwise classified. Includes such features as decking, swimming pool shells, and railroad rails and ties.
description	Text		Notes and descriptive information provided by the observer, if applicable. Descriptions are edited to correct typographical and grammatical errors, and to remove

Attribute	Data Type	Controlled Values	Definition
			irrelevant or personal information, such as property owner names and addresses, and so on.
fault_azimuth[1]	Text		Strike of the fault zone in degrees from true north (0–360). If qualified by a double asterisk (**), the fault azimuth is estimated by the compilers from the rupture map and used for slip calculations.
ss_displacement[1]	Text		Strike-slip displacement, the length of the horizontal component of total slip on the fault plane, in centimeters. If qualified by an asterisk (*) the value is reported as an approximation or represents some undocumented component of horizontal fault movement, such as separation normal to a faulted feature or piercing point separation. If qualified by a double asterisk (**), strike-slip component is computed by the compilers using a fault azimuth value estimated from the map.
ss_sense[1]	Text	RL or LL	Sense of strike-slip displacement, either reported or computed from slip vector information and fault azimuth. RL=right-lateral displacement; LL=left-lateral displacement.
ext_offset[1]	Text		The amount of horizontal opening (extension) measured normal to the fault plane, in centimeters. If qualified by an asterisk (*), value is an estimate. If qualified by a double asterisk (**), extension is computed by the compilers using a fault azimuth value estimated from the map.
comp_offset[1]	Text		The amount of horizontal shortening (compression) measured normal to the fault plane, in centimeters. If qualified by an asterisk (*), value is an approximation.
vert_offset[1]	Text		The vertical component of dip-slip displacement, in centimeters. If qualified by an asterisk (*), value is an approximation.
upthrown_side[1]	Text	N, S, E, W or not reported	If a vertical component of fault displacement is reported, this is the cardinal direction of the upthrown side. N=north side up; E=east side up; S=south side up; W=west side up.
trace[1]	Text		Identifies the fault trace (A-G) or region (H-V) where the observation is located.
origin[1]	Text		Interpreted cause of the ground deformation observed at the station, either inferred directly from the observation or from context based on fracture orientation, displacement sense, setting or nearby observations.
		Lateral spread	Surface cracks inferred to have been produced by lateral movement of a soil mass toward a free face, likely owing to shaking-induced liquefaction or shear failure of subsurface materials.
		Shaking	Ground deformation inferred to have been produced solely by shaking-induced settlement or slope failure (for example, slumps, soil falls, bank failures).

Attribute	Data Type	Controlled Values	Definition
		Tectonic	Ground deformation observed along a linear trend with a displacement sense consistent with the earthquake source mechanism. Right-lateral offsets may be observed directly or inferred from a pattern of left-stepping en echelon surface fractures. Tectonic surface rupture includes seismogenic rupture that has propagated to the surface from the earthquake source and slip resulting from shallow strain release triggered by shaking or changes in near-surface stresses from the earthquake.
		Uncertain	Fractures with orientations and displacement sense not consistent with the earthquake source mechanism, or isolated observations of ground deformation with no discernible lateral displacement. Features of uncertain origin that are associated with InSAR lineaments may in fact be from faulting where displacements are small, distributed, or overprinted by shaking-related settlement or pavement decoupling, or to shallow, secondary faulting that results from folding, distributed shearing and surface block rotations along these trends. Alternatively, these linear zones may simply reflect stratigraphic or structural boundaries controlling deep-seated gravity failures (for example, block glides and ridge-spread phenomena) or that separate different geologic materials that have settled differentially owing to shaking. Sites of ground deformation not associated with linear trends and that cannot otherwise be readily explained by typical earthquake-induced ground failure mechanisms (for example, liquefaction or shallow slope failure), are also included in this classification.

[1]This field is only present within the Observations table.

The Photos table includes EXIF metadata that is embedded within the digital image file for each of the individual photographs included in our compilation. More than 4,000 photographs were collected, of which more than 2,300 were retained after eliminating duplicate, poorly exposed, or non-geolocated images. All photo records in the Photos table are assigned to a station in the Observations table. Attributes stored in the Photos table are defined in table 2.

Table 2. Attribute definitions for the Photos table.

[Attribute names in bold are non-null fields]

Attribute	Data Type	Controlled Values	Definition
photoid	Integer		Unique identifier.
intid	Integer		Internal identifier. Links to the intid field of the Observations table.
photographer	Text		Last name of the individual who took the photograph. Full names and affiliations are listed on the report title page.
hires	Text		URL to the full resolution image.

Attribute	Data Type	Controlled Values	Definition
Fnumber[1]	Text		F-number (f-stop) or relative aperture for the photograph. F-number is the ratio of the lens' focal length to the diameter of the pupil.
create_date[1]	Text		Date and time the photograph was taken as recorded in the image file's EXIF data. Date is given as numerical year, month, and day separated by colons, followed by hour, minutes and seconds, also separated by colons (for example, 2014:08:24 11:45:19 represents August 24, 2014, 11:45:19 a.m.). Time of day is given in 24-hour notation (military time), local time (GMT-7). If the time is not embedded with the image file, create_date is assigned to the observation date of the associated station.
stn_lat	Float		Coordinates of the station associated with this photograph, in WGS84 datum.
stn_lon	Float		
gps_lat[1]	Float		Coordinates of the camera location (WGS84 datum), taken from the camera GPS or matched to a GPS device's track log based on the create_date.
gps_lon[1]	Float		
latitude	Float		Coordinates (WGS84 datum) used for the photo location. These typically are the embedded camera coordinates (gps_lat, gps_lon), unless significant error is noted in the location, in which case the coordinates are adjusted based on the compiler's best estimate. If there are no embedded camera coordinates, this is the location of the associated station.
longitude	Float		
gps_satellites[1]	Text		The number of GPS satellites used to compute camera location; provides a qualitative estimate of location accuracy.
gps_altitude[1]	Text		Altitude of the camera as provided by the camera GPS. Datum is specified in the value.
gps_image_direction[1]	Text		The azimuth of the camera look direction (0–360) in degrees. Datum for the azimuth (True North or Magnetic) is specified in the value.
imagesize[1]	Text		Dimension of the image in pixels, given as width × height (for example, 2,592x1,936).
shutterspeed[1]	Text		Image exposure time, in seconds.
focallength[1]	Text		Lens focal length, the distance between the lens and the image sensor when the lens is focused at infinity.
hyperfocal[1]	Text		Hyperfocal distance, the distance between a camera lens and the closest object that is in focus when the lens is focused at infinity.
fov[1]	Text		Field of view, the angular extent of the image.
digitalzoom[1]	Text		Indicates whether the image has been magnified digitally by cropping of the original image and interpolating the result back to the pixel dimensions of the original image. Values >1 indicate the degree of magnification.

Attribute	Data Type	Controlled Values	Definition
model[1]	Text		Camera make and model.
lenstype[1]	Text		Description of the camera lens make and model.
metermode[1]	Text		Light metering method for determining exposure.
		Average	Light is averaged across the entire frame to determine exposure.
		Center-weighted average	Evaluates light in the middle of the frame and surroundings and ignores the corners.
		Evaluative, Multi-segment, ESP	Manufacturer-specific terminology for default metering systems that evaluate light by dividing the frame into multiple zones and analyzing for dark and light tones, prioritizing the focus point.
		Spot	Only evaluates light around the focus point and ignores everything else.
whitebalance[1]	Text	Auto, Manual	Indicates whether the camera automatic white-balance adjustments were turned on (Auto) or off (Manual).
description	Text		Description of the image provided by the photographer.

[1]Value obtained from the EXIF data embedded within the original image file

In all, there are more than 1,200 stations where observations of ground deformation were made. Of these, displacement measurements were acquired at more than 270 stations, but for most, not enough measurements were recorded to fully define fault slip in three dimensions. More than 900 stations have photo documentation.

Accuracy of Location Data

Station locations were determined in the field using various instruments and methods, the most common of which were smartphones, mobile tablets, or cameras with embedded GPS chipsets. Location information was also collected using handheld GPS devices and by digitizing directly onto georeferenced base maps. Published studies comparing the horizontal accuracy of cell phones to standalone GPS devices have shown that GPS receivers are commonly more accurate than cell phones or tablets (Zandbergen, 2009), but that newer phones with assisted GPS can achieve similar accuracies and acquire a positional lock faster than standalone GPS devices (Jones and others, 2015). Horizontal accuracy can vary widely, from less than 2.5 m for standalone GPS devices, and from less than 10 to more than 200 m for cell phones and tablets, depending on model, cellular provider, satellite geometry, and local conditions (Jones and others, 2015).

During our compilation, we commonly noticed location discrepancies on the order of 10 m, comparable to those reported above, when comparing different observations at collocated sites, or when comparing reported coordinates to their “true” locations derived from high-resolution orthoimagery. In several cases, we noticed location discrepancies of more than several hundred meters. The largest errors appear to have been associated with incorrectly reported datums or where observations were recorded either with the GPS turned off or before the receiver acquired a positional lock. Cellular phones can acquire a lock quickly if the phone has a

cellular data connection, but often the user is not aware of whether the phone has a lock or not. Phones and tablets typically do not provide much information to the user about how the GPS is functioning, nor is that information recorded.

Although location errors on the order of 10 m are adequate for initial reconnaissance and fault-length evaluations, these errors are problematic when compiling observations onto post-earthquake orthoimagery and lidar data with sub-meter precision and resolution. For observations reported on a fault trace that was visible on post-earthquake lidar, InSAR, or orthoimagery, we adjusted the observation locations to align with fault traces mapped on the imagery, by using observer descriptions, photographs, and Google Maps Street View to constrain the adjustment. These adjusted stations are likely accurate to within a few meters, relative to the base imagery, and in most cases accurate to less than 1 m where there is sufficient documentation from ground photographs. For stations with insufficient documentation to inform any adjustment to the original, reported location, the original coordinates are maintained and the positional uncertainties of those stations are therefore unknown, but most likely on the order of 10 m. Both adjusted and original coordinates are recorded in the Observations, No Deformation Observed, and Photos tables.

Rupture Characterization

Aside from photographic documentation, text descriptions of fault rupture and ground deformation make up the bulk of the information recorded. Although several descriptions are quite detailed, oftentimes important information was not recorded directly, including time that an observation was made, fracture and displacement azimuths, and type and orientation of offset feature. This information could sometimes be inferred from accompanying photographs in context with airborne imagery or other descriptions, but in many cases this important information was lost.

Observations of ground rupture are time-sensitive, especially where afterslip is occurring. Although observation date was always reported, observation time, or the time interval during which observations were being made, was often not. Therefore, observation times are not formally reported here; however, each record in the Observations table and summarized in the appendixes includes the observation date, and origination times for photographs, where they exist, were extracted from the photo metadata, reported in the Photos table and presented in the appendixes; these photo times can be used to estimate observation times. Observers may have recorded times within their descriptions and if so, that information is preserved in the description attribute of the Observations table. It is emphasized that observation time is critical information that should be explicitly reported for all future post-earthquake observations.

The ability to observe and accurately measure fault slip is dependent in part on the materials being deformed and the type and geometry of the feature that is offset. Furthermore, the azimuth of the rupture and the azimuth of any recorded displacement are essential data to obtain along with displacement magnitude and sense. For this compilation, several offset feature classifications are defined and assigned to stations based on information obtained from airborne imagery and ground photographs. Details about the offset feature, if provided by the observer, are preserved in the description attribute of the Observations table. When not otherwise reported, fault azimuths and slip components for some observations were estimated by the compilers from airborne imagery and ground photographs as discussed below.

Station descriptions in the Observations table and appendixes include notes recorded by observers exactly as written, except for the following: (1) typographical or grammatical errors

were corrected; (2) notes not pertinent to the observation, names of property owners, addresses, or other personally identifiable information were removed; (3) compiler notes were added where appropriate; and (4) measured slip components, as they were originally described, were also added. Many observers took advantage of the voice-recognition capabilities of their smart phones and tablets to speed recording of descriptions. With voice recognition, observers could record data more efficiently, yet too often this resulted in transcribed descriptions that, unless corrected in real time by the observer, were partly or wholly unintelligible and could not be fully included. Until voice recognition technology improves sufficiently, it is suggested that, for speed on station, observers record sound clips that can be transcribed at a later time.

Slip Measurements

For the South Napa earthquake, predominant fault movement was horizontal with right-lateral strike-slip displacement. Locally there were dip-slip components, observed as vertical offsets and in features that expressed extension or compression normal to the fault strike. By measuring fault strike direction (fault azimuth) and the length, plunge, and azimuth of the slip vector,[4] all components of fault slip can be derived, including strike-slip displacement and displacement sense (fig. 2). In many cases, it is difficult to measure the slip vector attributes directly but the strike-slip displacement can still be derived through other methods: (1) if the horizontal distance and azimuth of the line that separates the piercing point can be measured, or (2) if the lateral separation of the offset feature (fig. 2) measured normal to the feature's azimuth and the feature azimuth are measured. The latter approach was used commonly in Napa where offset vineyard rows were used to derive horizontal fault slip.

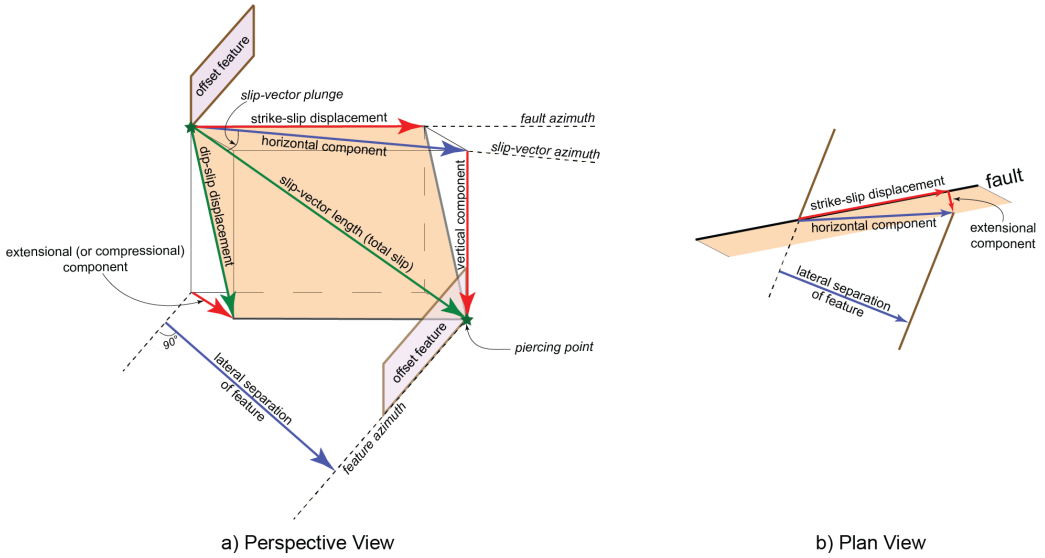

Figure 2. Perspective (*A*) and plan view (*B*) diagrams illustrating the various components of fault slip. Components in blue are commonly measured in the field; components in red are those recorded in the Observations table and listed in the appendixes. Components in green may be measured directly in the field but are commonly computed from other measurements.

[4]The slip vector is a line that connects a point on a linear feature (piercing point), with the equivalent point on the feature after it has been cut and moved apart by fault displacement (see fig. 2).

In the Observations table, strike-slip displacement is specifically recorded as the horizontal slip component, as this value can usually be computed from original measurements regardless of whether the observer measures and reports slip vector attributes, the horizontal component of displacement, or feature separation. However, where observers only reported an offset length and displacement sense (for example, 10 cm right-lateral) it is not certain as to which horizontal slip component was directly measured, or if the strike-slip displacement itself is being reported. If the fault azimuth and displacement or offset feature azimuth is not recorded, strike-slip displacement cannot be accurately computed even where it is clear how the horizontal offset is measured. For this compilation, the reported strike-slip displacement is denoted with an asterisk (*) where horizontal offset is measured but where it is not clear what component of horizontal displacement it represents, or if the measurement is identified by the observer as approximated or estimated. Because dip of the seismogenic fault appears to be steep at the surface at most sites, measurements of horizontal separation of the piercing point are likely to be quite close to the actual strike-slip displacement on the fault. Offset measurements made normal to linear features, however, will underestimate strike-slip displacement unless the feature is oriented perpendicular to fault strike.

Where we know the type of horizontal offset measured (for example, horizontal component or feature separation), and only the fault azimuth is missing, the fault azimuth can be estimated from lidar or airborne imagery to compute the strike-slip displacement. These strike-slip displacements are qualified by a double asterisk (**) in the Observations table. Vertical, extensional, and compressional components of fault slip were handled in the same way: for example, where the reported value is an estimate or there is uncertainty in the value, the measured values are qualified as with strike-slip displacement.

It is important to recognize that measured values for fault slip reported here are derived primarily from short aperture measurements using relatively low-precision devices such as tapes and hand compasses. Where faulting is distributed across a zone that is meters wide, these approaches likely underestimate total fault slip. For the South Napa earthquake, several studies have looked at both coseismic and postseismic slip at several localities with longer apertures and higher precision using terrestrial and mobile laser scanners and unmanned aerial vehicle synthetic aperture radar (UAVSAR) data (Brooks and others, 2015; DeLong and others, 2016). Results of these analyses demonstrate that block rotation and distributed slip did occur within several meters of visible fault rupture (Brooks and others, 2015; DeLong and others, 2016) and are likely not included in many of the measurements reported here.

Although various formats were used for collecting and reporting data, it is recommended that observers focus on the type and quality of data reported and identify and correct input errors prior to dissemination, reducing potential errors during compilation of the data.

Improving Future Post-Earthquake Observations

The South Napa earthquake response was one of the first times where post-earthquake reconnaissance data were mostly collected and disseminated electronically. These new advances have led to a substantial increase in the volume of data collected immediately after the event as well as the speed in which these data are disseminated. However, the current lack of standards and processes for digital data collection, coupled with the different types of software and data formats used, present new challenges to large-scale compilation efforts.

A notable advantage to collecting data digitally is that information only needs to be recorded once, which eliminates transcription errors and the time required to compile

handwritten observations and photographs before dissemination. However, that manual process did have one advantage in that it provided an opportunity for an observer to catch and correct input errors or inconsistencies in the data. Now that it is easy to disseminate recorded data automatically, it is critical that input errors are identified and corrected during the recording phase. This requires developing guidelines and processes for verifying the accuracy of recorded data before dissemination.

As described earlier, geologists collected information following the South Napa earthquake using various digital tools and software, and they disseminated their observations in several different data formats. Although these issues made the data compilation effort more challenging, software interoperability will no doubt improve in the future as these tools and software evolve. More important is to focus on developing guidelines for the types of field data that should be collected. Several groups have worked to develop field guides for data collection (Earthquake Engineering Research Institute, 1996), standardized data entry forms, and online data collection tools for post-earthquake investigations (for example, California Earthquake Clearinghouse, 2009; Clearinghouse Field Notes application, https://bayquakealliance.org/fieldnotes/). These efforts represent a good first step, but each approach is different, and it may not be appropriate to expect a single data standard or form to work well in all circumstances, given that every earthquake presents unique challenges to investigators. It is probably most important, therefore, to identify the minimum amount of information that should be collected during post-earthquake geologic reconnaissance so that the most important data and metadata do not go unrecorded. Toward that end, the following are suggested guidelines, based on our experience with the South Napa earthquake, for ensuring that critical information is not lost or misinterpreted:

1. For every observation made, the following information should be recorded:
    A. Date and time of observation (with specified time zone) including times of measurements and photographs. Observation time is particularly important for earthquakes where afterslip is observed or expected.
    B. Method used for determining location, including equipment used, map scale, image resolution, GPS equipment make/model if applicable, and the number of satellites along with the geometric dilution of precision (GDOP) for the measurement, if available. Users of mobile devices such as phones and tablets must be cognizant of potential limitations of the GPS receiver and in all cases users should verify the location prior to disseminating coordinate data.
    C. Names and affiliations of all field team personnel. This information is important if multiple individuals from the same field team submit data separately
    D. For photographs, in addition to location, time, and camera metadata (such as model, lens, and so on), look direction and estimated distance to the feature of interest. Photographs should also include a scale if documenting feature displacements.
    E. Text descriptions that are limited to objective observations and checked for typos (especially if recorded with voice recognition software).
    F. Types of equipment used for measuring lengths, azimuths, and angles.
2. When slip measurements are taken, the following information should be recorded:
    A. Type of offset feature where measurement is made (for example, soil, curb, fence).
    B. Width of the deformation zone over which slip is measured and whether the measurement represents minimum slip or not. Where slip is distributed across a zone

of en echelon faults and no offset feature crosses the entire zone, slip can be estimated by summing up slip vector measurements across individual en echelon fractures along a profile oriented normal to the overall fault zone.

C. Azimuth of the fault trace. If the zone consists of en echelon fractures, measurement should be of the zone azimuth, not the fracture azimuth.
D. Where piercing points are clearly identified, the azimuth, plunge angle, and length of the slip vector (fig. 2), or as many components of the slip vector as can be measured (for example, horizontal, vertical, fault normal), as well as displacement sense.
E. Where piercing points are not well defined, separation (measured normal to the offset feature), and azimuth of the offset feature.

3. In addition, it is important to include observations for locations where deformation was anticipated but not observed, such as along projected fault strike or where InSAR data indicates the presence of localized surface deformation.

Rupture and Ground Deformation Mapping

Field reconnaissance following the South Napa earthquake focused on documenting the extent of ground rupture, yet there was no systematic attempt to map fault rupture or ground deformation features in the field. An objective of this study was to compile field observations and integrate that information with post-earthquake airborne imagery, lidar, and InSAR interferograms to produce a large-scale digital map product (in Esri line shape file and KML formats) of surface faulting and ground deformation features.

Data Sources

Information from many sources was used to construct the rupture map, including large-scale maps drawn in the field, post-earthquake aerial photography, shaded relief images derived from post-earthquake lidar data, and InSAR interferograms. These data sources represent fault rupture and ground deformation features at notably different levels of detail and location precision. Rather than attempt to standardize a representation of fault rupture across the entire region, the maximum level of detail available for any given line on the map was preserved and the type (for example, field map, imagery) and provider of the source data are recorded as attributes for each line feature in the map. Where field maps existed for an area, those data were used. If field maps were not available, rupture was mapped on airborne imagery and then on lidar where applicable. Where rupture could not be observed in those datasets, lineaments observed in InSAR interferograms were used to map the location and extent of fault rupture and linear ground deformation features.

Field Maps

Because details of ground deformation are best observed in the field, large-scale field-derived maps provide the most detailed representation of ground rupture. Field maps were constructed by several observers in only a few limited areas (fig. 3) for specific purposes; for example, determining width, direction, and amount of rupture at pipeline crossings, identifying fault setback zones for upcoming construction projects, documenting displacements and fracture geometry in areas of distributed deformation, or delineating areas of bank failures. These data were produced in the field by mapping ruptures directly onto photo or topographic base maps or by walking along traces and recording positions using GPS receivers; the specific procedures

used were not always reported and various field map sources are distinguishable only by the author who provided the data.

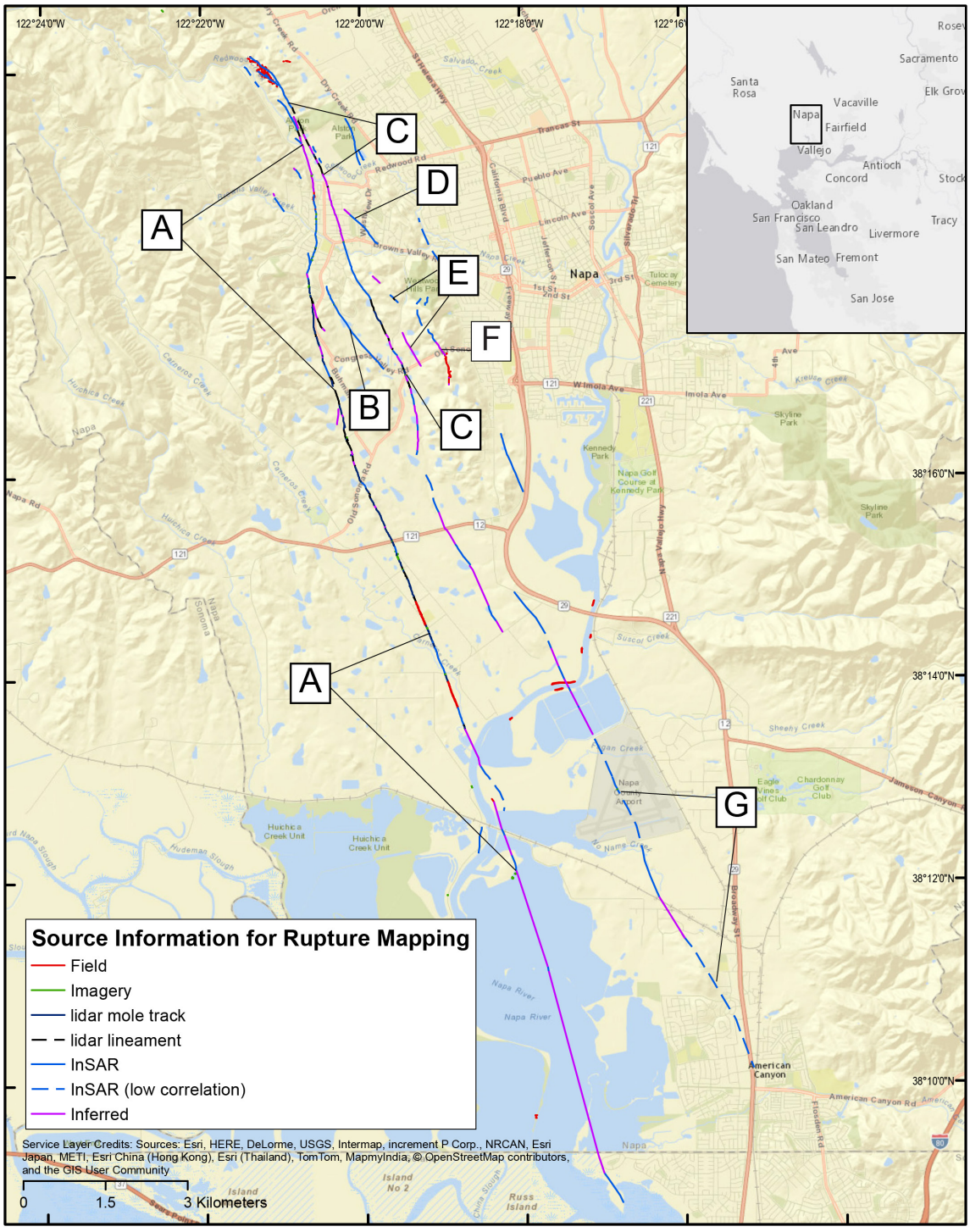

Figure 3. Map of ground deformation produced by the August 24, 2014, South Napa earthquake, showing the types of source information used for constructing the map. Categories shown in the legend are explained in table 3. A–G, principal tectonic traces discussed in this report. Inset shows location of map area relative to San Francisco (located ~50 km south) and other major northern California cities.

Maps were submitted as either GIS files or in hardcopy format. Hardcopy maps were georeferenced and digitized for inclusion. Linework is largely unedited from the original submissions, although in a few areas, line features may have been moved to more closely align with corresponding ruptures that were visible in the post-earthquake orthoimagery. Locations of the mapped ruptures are accurate to within several meters, depending on the map procedure used and base map scale. A representative example of the types of rupture detail captured in the field mapping is shown in figure 4.

Figure 4. Map of a portion of the fault rupture produced by the August 24, 2014, South Napa earthquake, showing a representative example of rupture detail mapped in the field. *A*, Fine-scale details of fault rupture on Trace A near Stone Bridge School (near stations 66–75, appendix 2, fig. 2.2) from field mapping by A. Lutz and C. Hitchcock, included in our rupture compilation, superimposed onto USGS/Towill orthoimagery flown on September 9, 2014. *B*, USGS/Towill orthoimagery of the same area without the overlying linework.

Post-Earthquake Airborne Imagery

In areas where surface displacements were large (>10 cm) and vegetation sparse, or where faulting crossed roads or other hardscape, the rupture could commonly be observed on orthorectified post-earthquake airborne imagery. Two sets of post-earthquake color imagery were used in this compilation:

1. Imagery acquired by Google Inc., on the afternoon of August 24, 2014 (less than 12 hours after the earthquake); image tiles from this dataset were provided to USGS by Google, Inc. under the Creative Commons CC BY 4.0 license. This imagery is available via Google's Earth application.

2. Imagery and lidar acquired by Towill, Inc., on September 9, 2014, under contract to USGS, CGS, the PEER-GEER engineering group, and the California Department of Water Resources (DWR). This dataset (USGS/Towill) is further described and available through the USGS Hazard Data Distribution System (HDDS) at https://hddsexplorer.usgs.gov/ (Hudnut and others, 2014).

Both image sets are of the same resolution (~15 cm) and comparable quality. The datasets have varying extents and sun angles, providing different levels of detail that complement each other. Because of its earlier acquisition date, the Google imagery captures the rupture before many road repairs were made, when only early postseismic slip had occurred. The USGS/Towill dataset, however, was acquired after a substantial amount of afterslip had occurred along the southern half of Trace A, which resulted in parts of the rupture zone being more readily visible on the USGS/Towill imagery. Both sets of images were used to compile the rupture map, relying on the image that best showed the fault rupture. An example of the post-earthquake imagery and interpreted linework is shown in figure 5.

Figure 5. Examples of post-earthquake airborne imagery used for the rupture compilation, showing expression of fault rupture on Trace A of the West Napa Fault System from about 200 m south of State Route 12/121 (stations 135–152, appendix 2, fig. 2.3). *A*, Google orthoimagery (~15-cm pixel resolution) acquired in the afternoon on August 24, 2014, less than 12 hours after the earthquake; *B*, USGS/Towill orthoimagery (~15-cm pixel resolution) acquired September 9, 2014; *C*, rupture interpretation from our compilation derived from imagery (yellow) and lidar (white) superimposed on USGS/Towill orthoimagery.

Post-Earthquake Airborne Lidar

Because most fault rupture produces small-scale micro-topography, the detailed elevation data obtained from the USGS/Towill lidar acquisition proved extremely valuable for identifying fault rupture that could not be observed on imagery. This was especially true where strike-slip faulting in unconsolidated material produced characteristic “mole tracks” (linear mounded zones that develop owing to off-strike shears) or where several centimeters or more of vertical offset was observed across the rupture. To use the lidar data for mapping, bare earth digital elevation model hillshade images (0.25-m pixel resolution) were produced using a low (20°) sun angle at azimuths of 55° and 235°. These images can be found in the companion data release (Ponti and others, 2019). Mole tracks, where present, are clearly discernible in the lidar hillshade imagery as positive topographic features (fig. 6), whereas small vertical offsets where no mole track is present appear as light or dark tonal lineaments in the hillshade imagery, depending on the lighting and scarp facing direction (fig. 7).

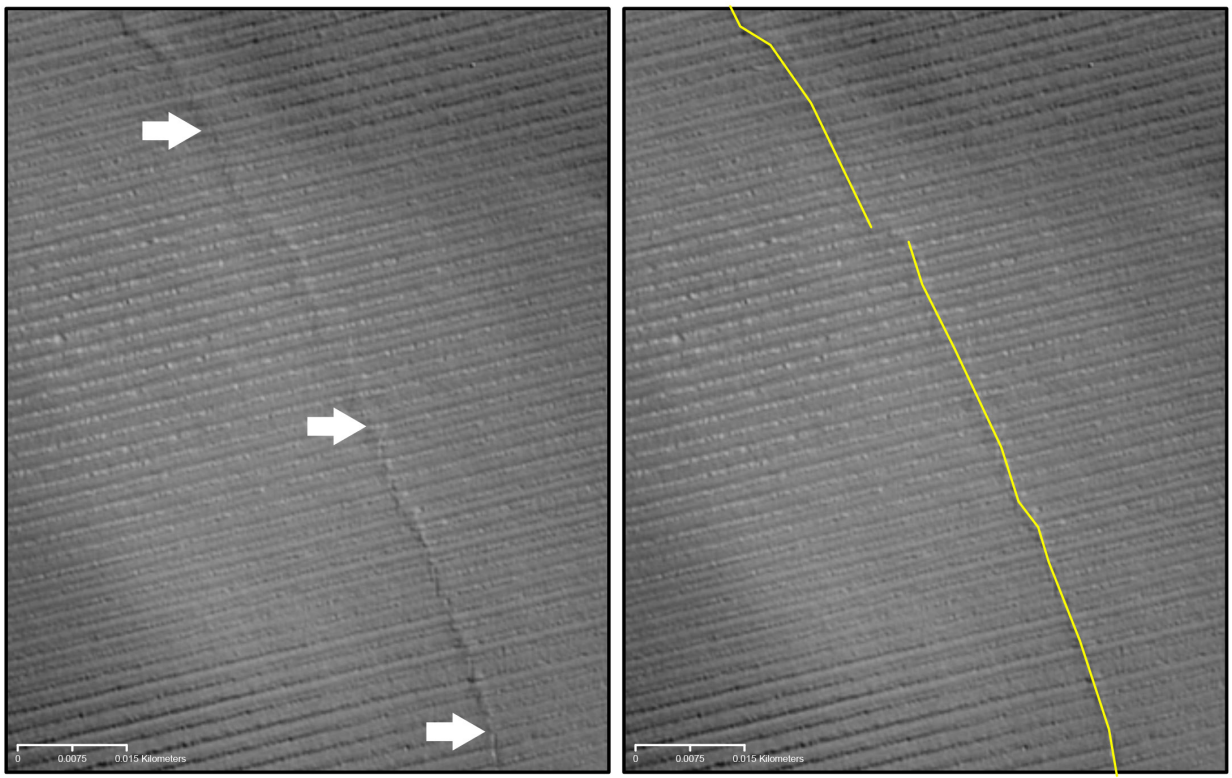

Figure 6. Lidar mole track showing expression of fault rupture on Trace A of the West Napa Fault System from a vineyard about 450 m north of State Route 12/121, located just north of stations 218–221 (appendix 2, figs. 2.3 and 2.4). *A*, The rupture is clearly expressed as a positive topographic feature (white arrows) in this USGS/Towill airborne lidar shaded relief image (light source from the northeast [55°], 20° above the horizon), defining a zone about 3 m wide. Strike-slip displacement here was about 30 cm when lidar was flown on September 9, 2014 (Lienkaemper and others, 2016), and offset of the vine rows is clearly visible. *B*, Same image as *A*, with interpreted linework from our rupture compilation. In most cases, we did not attempt to replicate fine-scale rupture details from the lidar.

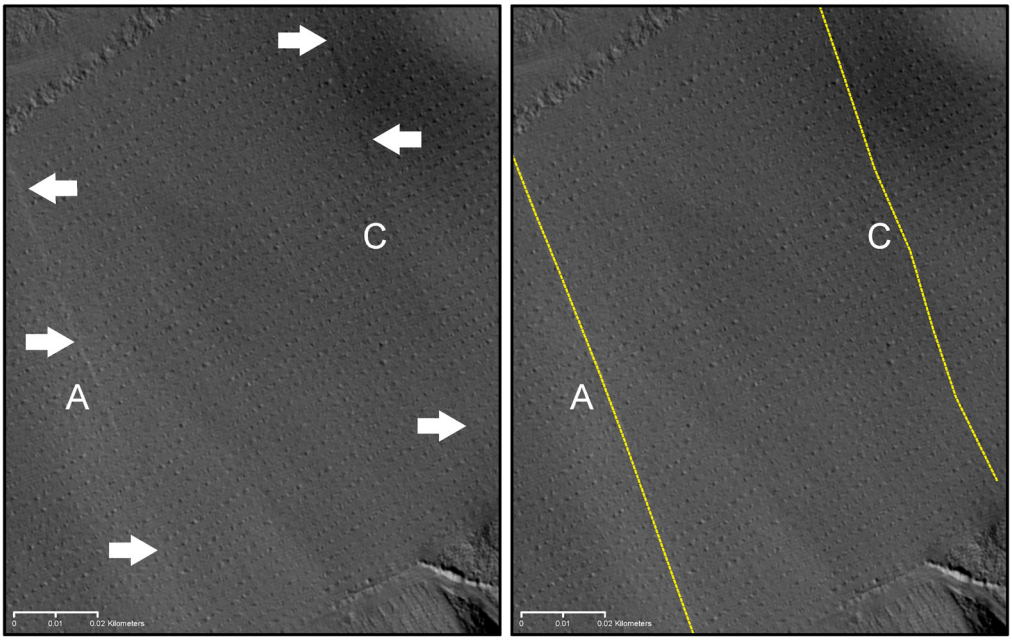

Figure 7. Lidar lineament showing expression of fault rupture on traces A and C (labeled) of the West Napa Fault System, at Hendry Winery, near the northern end of the rupture (near station 469, appendix 2, fig. 2.7, and near stations 699–702, appendix 4, fig. 4.3). *A*, Rupture is expressed as tonal lineaments (white arrows) in this USGS/Towill airborne lidar shaded relief image (light source from the northeast [55°], 20° above the horizon) that results from a small amount of west-side up vertical offset on Trace A, and east-side up vertical offset on Trace C, producing a graben between the two traces. Vertical offset was not noted or measured in the field; strike-slip displacement on Trace A in this area is negligible, but more than 4 cm on Trace C. *B*, Same image as *A*, with interpreted linework.

Synthetic Aperture Radar Interferometry

InSAR is a remote sensing technique for quantitatively measuring changes in the Earth surface over time. By conducting an interferometric comparison of pre- and post-earthquake radar images, deformation caused by the earthquake can be detected at a high level of detail and sensitivity (Rosen and others, 2000; Rosen and others, 2006; Donnellan and others, 2014). Post-earthquake field reconnaissance was influenced greatly by synthetic aperture radar (SAR) interferograms obtained from spaceborne and airborne platforms: the COSMO-Skymed X-band satellite (NASA, 2014), NASA's UAVSAR L-band aircraft (NASA, 2015), and the Sentinel-1A C-band satellite (European Space Agency, 2015). Of these, UAVSAR interferograms proved most useful to field reconnaissance efforts because, compared to the satellite data, the UAVSAR line-of-sight direction (nearly parallel to the strike of the West Napa Fault System) and lower incidence angles produced interferograms sensitive to small amounts of north-northwest–south-southeast directed strike-slip motion. Lineaments visible in the UAVSAR interferograms identify possible areas of fault rupture, and thus a substantial amount of the post-earthquake field reconnaissance effort involved searching for field evidence of deformation along these lineaments.

Fault rupture could not be verified on all of the UAVSAR lineaments that were field checked, however. Ground cracks and evidence of disturbance to compacted soil, pavement, curbs, and sidewalks were observed coincident with some UAVSAR lineaments but with

fracture orientations and displacements that were not consistent with a tectonic origin, indicative of other causes. Other lineaments proved not to have any visible evidence of ground movement, suggesting that deformation was buried or too small and (or) broadly distributed to have observable expression in the field.

The InSAR data proved crucial for compiling the rupture map in areas where surface faulting and ground deformation features did not have sufficient lateral continuity or displacement to be visible in either the imagery or lidar. In combination with the field observations, InSAR was used to identify potential fault zones and linear zones of deformation that were located off of the primary South Napa earthquake rupture, confirm connectivity of deformation between observation stations, and extend ground deformation into areas where no field observations could be made.

NASA/Jet Propulsion Laboratory's UAVSAR airborne repeat-pass interferometric SAR collects L-Band (24-cm wavelength) SAR images with a resolution of 1.9 m in range and 0.8 m in the azimuth direction (DeLong and others, 2016). UAVSAR flight lines run approximately perpendicular to the West Napa Fault System, and these interferograms are more sensitive to strike-slip deformation than the west- or east-looking satellite data. UAVSAR images were collected 87 days prior to the earthquake (May 29, 2014), 5 days post-earthquake (August 29, 2014), and 59 days post-earthquake (October 22, 2014) (NASA, 2015). These data were processed as interferograms (~6-m pixel resolution) that display the change in radar phase (distance) between a point on the ground and the aircraft instrument during the time interval between images (Rosen and others, 2000; Rosen and others, 2006).

Interferograms were selected for each UAVSAR flight line to represent the preseismic period (Interval 1: typically October 13, 2013–May 29, 2014, see table 3); the interval spanning the earthquake (Interval 2: May 29, 2014–August 29, 2014), which includes both coseismic rupture and the first 5 days of postseismic activity; and the postseismic interval (Interval 3: August 29–October 22, 2014) (NASA, 2015). For the southernmost ~2 km of Trace G, an interferogram (~7-m pixel resolution) derived from the European Space Agency's Sentinel 1A C-Band satellite data obtained on August 7 and 31, 2014, was used (European Space Agency, 2015). Specific interferograms used for mapping are shown in table 3.

Table 3. UAVSAR and InSAR interferograms used for this study.

Interval	Date range	Interferogram
1	10/31/13–5/29/14[1]	UAVSAR SanAnd_23511_13165-005_14068-001_0210d_s01_L090_01 (line 23511)
		UAVSAR SanAnd_05510_13165-004_14068-000_0210d_s01_L090_01 (line 05510)
		UAVSAR SanAnd_05512_12017-009_12128-002_0201d_s01_L090_01 (line 05512)
2	5/29/14–8/29/14[2]	UAVSAR SanAnd_23511_14068-001_14128-002_0092d_s01_L090_02 (line 23511)
		UAVSAR SanAnd_05510_14068-000_14128-003_0092d_s01_L090_01 (line 05510)
		UAVSAR SanAnd_05512_14068-002_14128-005_0092d_s01_L090_01 (line 05512)
		Sentinel 1A 20140807_20140831_7m_phs_raw
3	8/29/14–10/22/14	UAVSAR SanAnd_23511_14128-002_14157-007_0054d_s01_L090_01 (line 23511)
		UAVSAR SanAnd_05510_14128-003_14157-006_0054d_s01_L090_01 (line 05510)
		UAVSAR SanAnd_05512_14128-005_14157-008_0054d_s01_L090_01 (line 05512)

[1]Except for line 05512 from 4/18/12–11/5/12

[2]Except for Sentinal 1A from 8/7/2014–8/31/2014

Shallow faulting or other ground deformation produced by the earthquake is expressed on Interval 2 and Interval 3 interferograms as lineaments produced by fringe dislocations or substantial changes in radar phase over a short distance (fig. 8). Most lineament mapping was performed on Interval 2 interferograms, although Interval 3 interferograms were used along along Trace A where coseismic slip was high. Preseismic (Interval 1) interferograms were used as a check on the mapping to ensure that mapped lineaments were not associated with non-seismic causes.

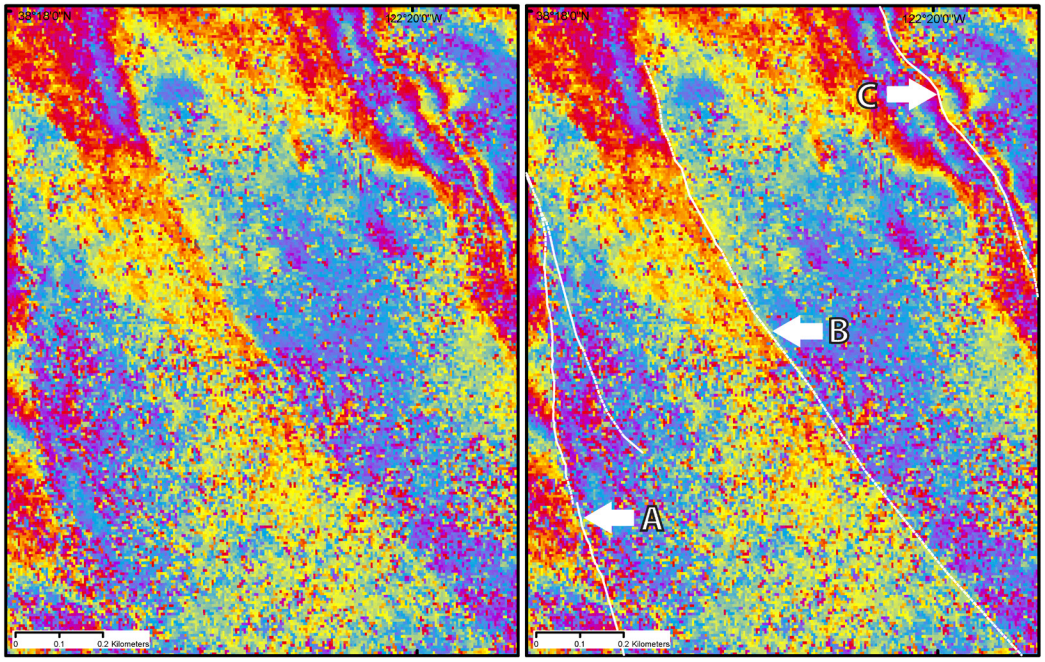

Figure 8. UAVSAR wrapped phase interferogram (line 23511) for a portion of the West Napa Fault System that ruptured in the August 24, 2014, South Napa earthquake. The interferogram is derived from data collected on May 29 and August 29, 2014 (Interval 2), and was used to aid rupture mapping where rupture could not be detected on airborne imagery or lidar shaded relief images. *A*, Interferogram centered over the Trace B lineament (fig. 1); color spectrum from red to violet represents a 2π change in phase. *B*, Same image with interpreted traces A, B, and C (labeled with arrows).

Interpretation of ground deformation from UAVSAR images is complicated by distributed or buried deformation that can "blur" a lineament. In addition, apparent lineaments can also be produced by decorrelation of the radar images in certain areas, mostly caused by changes in land use or vegetation, and uncertainties in topographic models and refractive variability of the atmosphere that introduces random phase distortions (Rosen and others, 2006; DeLong and others, 2016). To reduce the subjectivity of our interpretations, InSAR lineaments were included in our rupture and ground deformation map only where they represent extensions of surface faulting as confirmed from ground observations, are associated with at least one field observation of ground deformation (regardless of origin), or are coincident with previously mapped traces of the West Napa Fault System. In addition, mapped lineaments that traverse or are directly adjacent to areas of low correlation (correlation coefficient <0.4, from UAVSAR COR files) are specifically identified.

Fault rupture and linear zones of ground deformation mapped from UAVSAR lineaments are typically not well expressed in the field, and in many areas, no surface rupture was observed. Evidence for ground deformation is discontinuous along most lineament trends, appearing primarily where there is brittle hardscape, such as curbs or asphalt roadways, but with fracture orientations and displacements that were not consistent with a tectonic origin. Lack of expression may be due to several factors, including low total displacement that is not manifested as brittle deformation in natural soils, deformation distributed across a zone several meters or more in width, shallow deformation that did not reach the ground surface, or a combination of the above. Observations of surface displacements along UAVSAR lineaments that are not collocated with previously mapped faults or extensions of observed fault rupture mostly lack clear evidence of tectonic faulting. Although the linear nature of these zones suggests faulting as cause for the deformation, these lineaments could also be induced by shaking or a result of secondary tectonic deformation.

Rupture Map and Associated Attributes

Linework representing fault rupture and linear ground deformation features interpreted from airborne imagery, lidar, and InSAR interferograms are combined with digitized field mapping into an Esri Shapefile and a KML file; both are published in the companion data release (Ponti and others, 2019). This linework is symbolized in report figures and appendixes according to various attributes. In addition to attributes that identify the source information type and provider, each line feature also contains attributes that identify the feature's inferred origin (for example, tectonic, shaking, or uncertain) based on field observations and other factors such as rupture continuity and surface expression. Definitions of the rupture map attributes are given in table 4.

Table 4. Attribute definitions for rupture map linework.

[Attribute names in bold are non-null fields]

Attribute	Data Type	Controlled Values	Definition
OBJECTID	Object ID		Unique identifier—Esri shapefile only.
Type	Text		The type of source information used to construct the linework.
		Field	Rupture segments were mapped directly in the field. Linework was then hand-digitized into the feature class or, if provided digitally, was digitally merged into the feature class.
		Imagery	Mappable rupture segments that were identified from ortho-rectified post-earthquake aerial imagery (see text).
		Inferred	Segments of surface or near surface rupture that are inferred to be continuous along trend between observation stations or ends of observed rupture segments, including possible rupture that occurred subaqueously. Rupture was not or could not be observed in the field, and cannot be confirmed from aerial imagery, lidar data, or InSAR data.
		InSAR	Segments of inferred surface or near surface rupture that are mapped from lineaments in UAVSAR or Sentinel-1A interferograms. Lineaments included in this compilation are

Attribute	Data Type	Controlled Values	Definition
			limited to those that extend known fault rupture, where ground deformation was observed in the field along the lineament trend, or where the InSAR lineament is coincident with previously mapped fault traces.
		InSAR (low correlation)	As above, but defining areas where the InSAR lineament traverses across regions where the interferogram correlation coefficient is less than 0.4, as derived from UAVSAR COR files. This type defines areas where there is a larger uncertainty in both the location and continuity of ground deformation.
		Lidar mole track	Rupture segments mappable from hillshade imagery generated from post-earthquake lidar data (see text), and expressed as small-scale topographic ridges (moletracks).
		Lidar lineament	Rupture segments mappable from hillshade imagery generated from post-earthquake lidar data (see text), and expressed as tonal lineaments.
Provider	Text		For Type=Field, the last name of the individual who produced the linework. Full names and affiliations are listed on the report title page. For rupture segments mapped from imagery, lidar data, or InSAR data, this field holds the source imagery information.
Date	Date		For Type=Field, the date that the rupture segment was mapped in the field; for airborne imagery and lidar data, the date that the data were acquired; for InSAR data, the date of the most recent radar acquisition.
Origin	Text		Inferred cause of the mappable deformation feature, based on ground observations and other factors such as rupture continuity, surface expression, and afterslip.
		Shaking	Mappable fractures inferred to have been produced solely by shaking-induced shallow slope failures and lateral spreads. Linear fractures represent head scarps of lateral spreads and landslides; closed lines bound regions of small-scale slumps, soil falls, and bank failures.
		Tectonic	Mappable fractures and related deformation along linear trends and having displacements consistent with the earthquake source mechanism, which in this case is dominantly right lateral strike slip. Right-lateral offsets may be observed directly in the field or on imagery or lidar data or inferred from a pattern of left-stepping en echelon surface fractures. Tectonic surface rupture includes both seismogenic rupture that has propagated to the surface from the earthquake source and slip resulting from shallow strain release triggered by shaking or changes in near-surface stresses from the earthquake.
		Uncertain	Rupture segments mapped in the field and (or) associated with UAVSAR lineaments and where fracture trends and displacements measured in the field were not consistent with the earthquake source mechanism nor were they readily

Attribute	Data Type	Controlled Values	Definition
			attributable to typical earthquake-induced ground failure mechanisms such as liquefaction or shallow slope failure.
Trace	Text	A-G, NA	Designation of trace referred to in this report. Tectonic rupture segments are labeled A–G. Rupture segments of shaking or uncertain origin are assigned NA.
Afterslip	Text	Yes, No, Possible, Unknown	Designation of whether the trace likely experienced postseismic creep following the earthquake based on UAVSAR interferograms from the postseismic interval. Yes= a distinct postseismic UAVSAR lineament is associated with the rupture segment; No=no postseismic UAVSAR lineament was observed; Possible= a weak or "blurred" lineament appears to be associated with the mapped rupture segment; Unknown = parts of Trace A where possible fault rupture is subaqueous and cannot be observed.

As mentioned previously, linework obtained from field mapping provides the most detailed representation of ground rupture, although the absolute accuracy of the rupture locations may vary depending on the base materials and techniques used by the various mappers. The high resolution (0.15-m pixel resolution) of the USGS/Towill imagery and lidar data, coupled with extensive ground control used to obtain these datasets (Hudnut and others, 2014), results in the most accurately located linework, although fine-scale details of the rupture as seen in the imagery and lidar data were not always replicated. The Google imagery has variable registration discrepancies, of as much as 10 m, relative to the USGS/Towill imagery. Linework mapped on Google imagery in areas where the discrepancy was more than 1 m was manually shifted to align with corresponding features in the USGS/Towill imagery. Although this improves the overall accuracy and consistency of the dataset, linework derived from Google imagery likely has a larger uncertainty, with respect to location, relative to the USGS/Towill dataset. UAVSAR and InSAR interferograms only show the location of fault rupture and ground deformation and do not preserve any fine-scale rupture details. The lower resolution of these images (~6-m pixel resolution), coupled with the effects of decorrelation, results in a larger uncertainty in the location of deformation features, on the order of 10 m or more, relative to other data sources.

Rupture features inferred to be of tectonic origin display mapped patterns or are associated with field observations that indicate right-lateral strike-slip displacement consistent with the earthquake source mechanism. Seismogenic fault rupture (for example, rupture that has propagated to the surface from the earthquake source) is not distinguishable from shallow slip that may have been triggered by earthquake shaking or changes in near-surface stresses (Donnellan and others, 2014).

Rupture features classified as uncertain in origin typically lack measureable displacement or a consistent sense of displacement along strike, and are commonly seen only in pavement or compacted substrate, but cannot be readily explained as resulting from commonly recognized earthquake-induced ground failure mechanisms, such as liquefaction or shallow slope failure. Ground deformation classified as uncertain in origin may in fact be due to tectonic faulting, with surface displacements too small and (or) too broadly distributed to be readily discernible in the field. These features may also be the result of secondary tectonic origin in response to rotation, folding or distributed shear, or could result from ground shaking in the form of differential

subsidence owing to variable subsurface materials, pavement decoupling, or from deep-seated, structurally controlled gravity-driven failures (for example, block glides or ridge-spread phenomena).

Rupture features inferred to be caused by shaking can be reasonably associated with shaking-induced shallow slope failures and lateral spreads, based on fracture morphology, displacement sense and topographic/geologic setting. These linear fractures typically represent head scarps of lateral spreads and landslides. Also included are closed lines that bound regions of small-scale slumps, soil falls and bank failures identified from field reconnaissance.

Characteristics of Surface Faulting

Overview

Considering its moderate magnitude, the South Napa earthquake is notable for producing large surface displacements and widely distributed surface rupture. Right-lateral, strike-slip surface faulting was identified on six subparallel fault traces within a zone about 2 km wide and more than 21 km long. As evidenced from the mapped pattern of rupture and ground photos included in this report (appendixes A–G), most surface rupture is expressed as disconnected left-stepping en echelon fractures several meters or more in length with measurable dextral slip. Where slip exceeds 30 cm, many left-stepping en echelon breaks become connected, with greater topographic expression and mole track development. Where slip is less than 10 cm, observed surface rupture is commonly discontinuous and manifests as single fractures on hard surfaces such as roads and sidewalks and loose or heavily vegetated soils.

The largest surface displacements are confined to Trace A south of Browns Valley and north of the epicenter (fig. 9). This observation is consistent with rupture models derived from inversion of seismic waveforms, GPS data, and InSAR data (Dreger and others, 2015; Floyd and others, 2016) that indicate that seismogenic rupture likely propagated upward and to the north from the hypocenter along this trace. These same studies also conclude that some slip occurred 5–10 km southeast of the hypocenter at a depth shallower than 2 km (Dreger and others, 2015; Floyd and others, 2016). Although ground observations are largely lacking or equivocal south of the Napa River, both coseismic and postseismic UAVSAR lineaments support the conclusion that dextral slip along Trace A extended as far south as Slaughterhouse Point (fig. 1; DeLong and others, 2016), for a total rupture length of more than 21 km.

On secondary traces B–G dextral slip does not exceed 8 cm (fig. 9). Field measurements of strike-slip displacement taken shortly after the event generally show that the largest displacements on traces B–E are near their northern ends (fig. 9), closest to Trace A, north of the slip maximum observed on Trace A. The proximity of traces B–E to Trace A indicates that these faults may connect at shallow depths, and the larger displacements in the north suggest that a small amount of seismogenic slip may have transferred to these structures from Trace A. Trace F, where the largest observed displacements are along its southern half farthest from Trace A, is an exception. Trenches excavated across Trace F show evidence for significantly larger fault separation during several prior Holocene events (Seitz and others, 2015) and suggest that Trace F may act independently from Trace A. Although the question of triggered versus primary slip on the secondary faults remains unresolved, overall it appears that slip transfer from Trace A to the secondary traces, if any, was limited.

Figure 9. Map of tectonic surface faulting produced by the August 24, 2014, South Napa earthquake, showing selected sites of maximum right-lateral strike-slip displacement (in centimeters) obtained from field measurements (white boxes), and previously mapped Quaternary-age strands of the West Napa Fault System. Only a selected set of previously mapped faults are shown for clarity; where different reports map the same feature, the earliest mapping is shown. Labels with asterisks are either approximate values or a

component of horizontal slip that may not be parallel to fault strike. Labels with double asterisks are strike-slip displacements computed by the compilers using an estimate of the fault azimuth. Displacement on Trace G was not measured in the field, but was estimated to be about 1 cm (Timothy Dawson, California Geological Survey, personal communication, 2014) and likely no greater than a few centimeters (DeLong and others, 2016). Inset shows location of map area relative to San Francisco (located ~50 km south) and other major northern California cities.

Afterslip

Prior to the South Napa earthquake, no interseismic creep had been detected along the West Napa Fault System (Galehouse and Lienkaemper, 2003). Nonetheless, evidence of postseismic creep (afterslip) following the South Napa earthquake was observed from about 2.5 to 9 km north of the epicenter in areas underlain by alluvial deposits. This afterslip only occurred on Trace A, which had varying amounts of postseismic and coseismic slip along strike (DeLong and others 2016; Lienkaemper and others, 2016). Ultimately, postseismic slip exceeded coseismic slip between the Napa River and Henry Road. (Lienkaemper and others, 2016; see fig. 1 for locations).

Segments of Trace A with high coseismic slip experienced less afterslip than those located closer to the epicenter with lower coseismic slip (DeLong and others 2016). Maximum coseismic slip (46 cm) from the South Napa earthquake, located 10.4 km north of the epicenter, is nearly equal to the peak combined coseismic and postseismic slip (47 cm) measured 6 km north of the epicenter 1 year after the South Napa earthquake (DeLong and others, 2016; Lienkaemper and others, 2016). InSAR data confirm the presence of afterslip along Trace A, including evidence for a small amount of afterslip occurring as far south as Slaughterhouse Point (fig, 10). Consistent with field observations, InSAR data show no evidence of afterslip on any of the other fault traces activated by the South Napa earthquake.

Both InSAR and ground observations show that afterslip did not extend north into Browns Valley (fig. 11). The northern terminus of afterslip is several hundred meters north of where the strike of Trace A shifts abruptly to a northeast azimuth. Possible afterslip may occur along a faint, approximately 200-m-long UAVSAR lineament that appears to intersect Trace A precisely where afterslip on Trace A ceases. No observations of faulting exist precisely along this trend, but the area near and north of this faint lineament experienced substantial distributed pavement and sidewalk damage, possibly related to distributed deformation or focused, intense ground motions. These observations are suggestive of a possible set of structures in this area that serve to distribute and accommodate Trace A slip and pose questions as to how slip may propagate to faults to the north.

The small displacements and lack of afterslip on Traces B–G suggest that rupture on these traces may have resulted from triggered shallow slip (Donnellan and others, 2014), rather than being connected at depth to the seismogenic fault. Dreger and others (2015), however, conclude that the rupture configuration could be compatible with a flower structure at depth. It is possible that faults may connect at shallow depths at the northern end of the rupture where they approach each other (fig. 1). Geodetic data interpreted by Floyd and others (2016) indicate minor post-seismic slip at depth along Trace G near the Napa County Airport, suggesting a delay in deeper slip following immediate triggered slip. The small displacements on the secondary traces make it difficult to differentiate between connected and triggered slip. However, because slip magnitudes are comparatively low on the secondary traces, it is apparent that substantial slip on Trace A did not step over to the secondary traces.

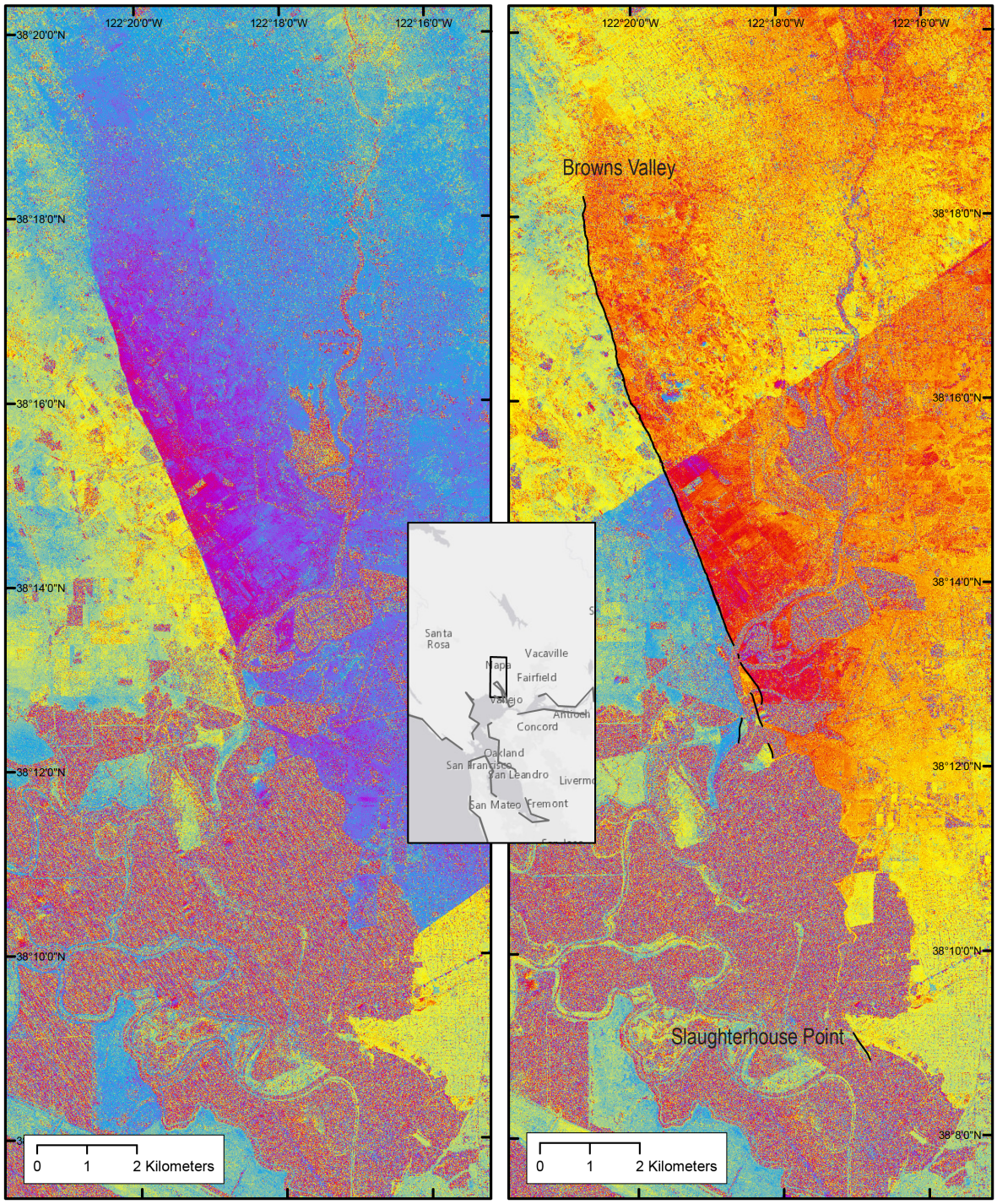

Figure 10. UAVSAR wrapped phase interferograms from the postseismic interval of the August 24, 2014, South Napa earthquake, between August 29 and October 22, 2014 (Interval 3). Inset shows area of figure. *A*, images from flight lines 23511 (north) and 05510 (south). *B*, images from flight lines 05512 (north) and 05510 (south). Black lines show the extent of the rupture and evidence for afterslip, as interpreted from the UAVSAR interferograms. Afterslip is confined to Trace A south of Browns Valley and apparently extends as far south as Slaughterhouse Point.

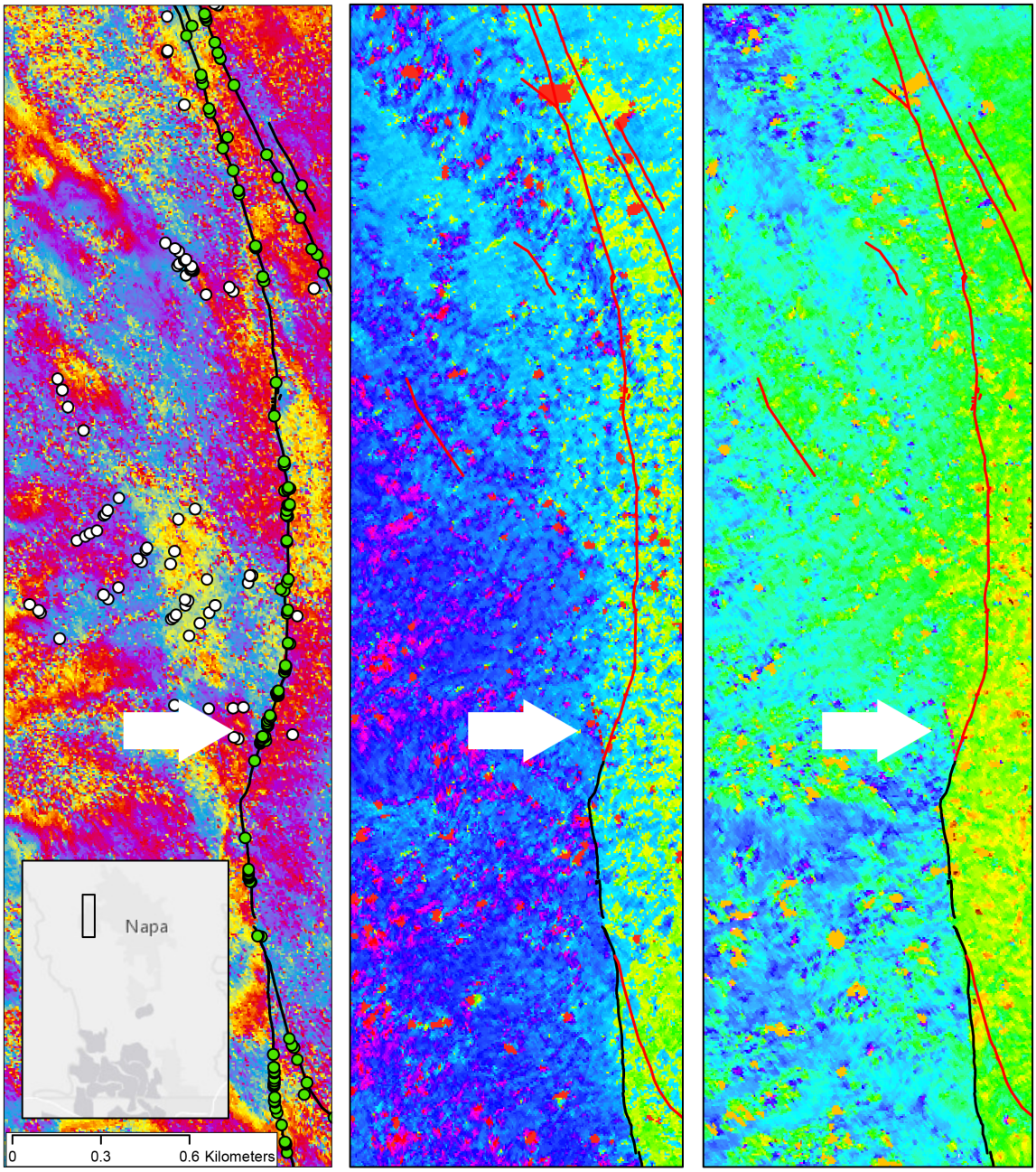

Figure 11. UAVSAR interferograms, mapped fault rupture, and observation stations near Browns Valley, California. Inset shows area of figure. *A*, Fault rupture (black) and observations of surface rupture of tectonic (green circles) and uncertain (white circles) origins, are overlain on the UAVSAR wrapped phase interferogram that contains the coseismic signal from the South Napa earthquake from flight line 05512 (Interval 2). Color spectrum from red to violet represents a 2π change in phase. Arrow points to a possible approximately 200-m-long lineament that branches off of Trace A about 200 m north of where the strike of Trace A shifts abruptly to the northeast. Near this lineament, white circles represent sites of damaged hardscape. *B*, Fault rupture overlain on the postseismic-interval (Interval 3) UAVSAR unwrapped phase interferogram from flight line 23511. Color spectrum from red to violet represents range change from 8.9 to -11.1 cm. Fault rupture line color indicates whether afterslip occurred along the trace (black, afterslip; red,

no afterslip), as interpreted from postseismic UAVSAR interferograms. Afterslip appears to cease along Trace A where the short coseismic (Interval 2) UAVSAR lineament intersects (arrow). A faint lineament (dotted), consistent with dextral slip along this trend, possibly indicates that afterslip continues along this short lineament west of Trace A. *C*, Fault rupture overlain on the postseismic-interval (Interval 3) UAVSAR unwrapped phase interferogram from flight line 05512. Color spectrum from red to violet represents range change from 9.7 to -16.4 cm. A faint lineament as in *B* (dotted line) is seen in this interferogram as well. Sharp gradations not annotated are likely due to vegetation and other cultural features.

Summary Descriptions

Trace A

Trace A is the surface expression of the seismogenic fault that produced the M_w 6.0 South Napa earthquake; most of the coseismic slip and all of the postseismic slip occurs along this trace. Rupture can be tracked for more than 21 km from Slaughterhouse Point (fig. 1, appendix 9, fig. 9.1) north to approximately 0.4 km past the northern boundary of Alston Park. About 7 km of the rupture zone north from Las Amigas Road had previously been recognized as a Quaternary-active fault (fig. 9; Bryant, 1982; Wesling and Hanson, 2008), but no active faults had been identified along the trace north through Browns Valley nor south toward San Pablo Bay.

There is no definitive field evidence for faulting along approximately the southernmost 7.5 km of Trace A, which is mostly covered by water and salt marsh. Instead, evidence for surface faulting derives from discontinuous UAVSAR lineaments within marshy areas that have inferred displacements consistent with both coseismic and postseismic dextral slip totaling less than 10 cm (DeLong and others, 2016). Although most of this area is underwater, tectonic rupture is inferred to be continuous and associated with Trace A from the Napa River (stations 9–13) south to Slaughterhouse Point, primarily owing to the presence of afterslip (fig. 1). Ground cracks oriented parallel to and coincident with Trace A were observed locally in salt marshes south and east of the Napa River (stations 6–13), although no definitive fault displacement was recognized. Faulting appears complex in the region between Bull Island and Green Island, as there are several subparallel lineaments present that all show postseismic slip (appendix 2, fig. 2.1). Although it is inferred these lineaments are on fault traces that are all connected to the principal seismogenic fault at fairly shallow depths, it is unclear exactly how or if these traces connect at the ground surface.

Definitive right-lateral surface faulting was observed about 350 m northwest of the Napa River (stations 14–17, appendix 2, fig. 2.1), and fault rupture progressively becomes more prominent as slip generally increases to the northwest. From South Avenue northward to State Route 12/121, the fault trace is linear, striking approximately 340°, with rupture well expressed as a series of closely spaced en echelon breaks and disconnected mole tracks that span a zone as wide as about 6 m (appendix 2, figs. 2.2 and 2.3). This area of the fault zone also displayed substantial afterslip, causing transtensional en echelon fractures to notably expand in the first few days following the event (stations 141–144, appendix 2, fig. 2.3).

North of Old Sonoma Road, fault strike changes slightly to a more northerly trend (~346° azimuth). The trace becomes more sinuous and surface expression of the rupture becomes more subdued. This may be due to an apparent reduction in slip between Old Sonoma Road and Henry Road, where measured slip on the day of the earthquake was less than 2 cm (station 258, appendix 2, fig. 2.4). Although substantial afterslip occurred at Henry Road following the

earthquake, total slip measured from alignment arrays persisted as a localized slip minimum (Lienkaemper and others, 2016; DeLong and others, 2016). In contrast, total displacements derived from UAVSAR data along the rupture 57 days after the event reached a maximum near Henry Road (DeLong and others, 2016). This apparent discrepancy may be due to a broad zone of distributed, non-brittle deformation at the ground surface in this area, observable in the InSAR data, but not captured by the shorter aperture alignment arrays.

At 0.5 km north of Henry Road, fault slip is observed to increase to more than 40 cm (station 270, appendix 2, fig. 2.4), but farther north, for about 1 km between stations 291 and 292 (appendix 2, figs. 2.4 and 2.5) fault slip may decrease or be distributed over a broad zone as the rupture is intermittently difficult to follow, especially where parts of it are likely obscured beneath landslide deposits. North of station 292, fault strike changes to a northerly trend (~355°), and for about 1 km to Leaning Oak Drive (stations 337–354, appendix 2, fig. 2.5), fault rupture occurs as very well developed, connected en echelon fractures, prominent mole tracks, and common transpressive deformation with up-to-the-west vertical displacement consistent with the local topography (stations 301–330, appendix 2, fig. 2.5). Transpressive deformation along with a change in fault strike to the north implies a substantial clockwise rotation of the fault slip vector in this region (from northwest to north-northeast), which may be an indication of interaction with another fault at depth. The largest fault displacements (>30 cm) were measured along this stretch of the rupture. The best constrained measurement (fig. 12, station 298, appendix 2, fig. 2.5) had a total slip of 46 cm (44.3 cm of strike-slip displacement, 10 cm of vertical displacement, and 7 cm of compression), with nearby estimates of slip of as great as 60 cm (station 328, appendix 2, fig. 2.5).

Figure 12. Photograph showing offset driveway at station 298 (appendix 2, fig. 2.5) where the maximum coseismic slip on Trace A (46 cm) of the West Napa Fault System was measured on August 25, 2014; view is to the southeast. Orientation of the driveway relative to the fault strike (yellow line) was such that two adjacent concrete slabs moved opposite to each other on either side of the fault, separating at a joint with

no rotation. The slip vector (white arrow) is slightly oblique to the fault strike producing compression that can be seen in the soil near the left edge of the lower slab where that slab "plowed" into the adjacent soil.

About 275 m north of Leaning Oak Drive, between stations 355 and 356 (appendix 2, figs. 2.5 and 2.6), the strike of the rupture abruptly changes to the northeast (20°). At this point, the rupture enters the Browns Valley subdivision where anomalous ground disturbance, typically expressed as pavement cracks, tented sidewalks, damaged curbs, and small fractures in compacted soil with no displacement sense, caused considerable damage to buried infrastructure and homes, despite a significant reduction in measured fault slip (for example, ~15 cm near station 374, appendix 2, fig. 2.6). The abruptness of the strike change suggests slip transfer along Trace A to a different fault, and afterslip on Trace A ceases about 200 m north of this point. North of Sandybrook Lane (station 402, appendix 2, fig. 2.6), strike of the rupture changes to approximately due north, and then gradually rotates counterclockwise to a strike of approximately 345° at Redwood Road. Along this segment of the rupture, slip gradually decreases from about 12 cm at station 402 to no more than a few centimeters at Redwood Road (station 443, appendix 2, fig. 2.6).

From Redwood Road, for about 1.5 km to the northern terminus of Trace A (appendix 2, fig. 2.7), rupture is visible on the ground as intermittent, en echelon fractures only a few meters in length, with little measurable slip. A small amount of west-side-up vertical displacement is evident in lidar imagery within a vineyard just south of Alston Park (fig. 7), but otherwise, the rupture is only traceable as a UAVSAR lineament.

Trace B

Rupture on Trace B is the surface expression of a short fault segment that likely connects Trace A to Trace C at depth. It was first identified from UAVSAR interferograms and then confirmed as a tectonic fault based on subsequent field investigations. The UAVSAR lineament that defines the Trace B rupture is curvilinear, about 2 km long, and has an average strike of approximately 325°. Surface expression of faulting appears as intermittent cracks and buckles in curbs, walkways, and asphalt along the lineament trend. Over most of the southern two-thirds of the lineament, there is no measurable displacement. The best evidence for tectonic faulting is at Alpine Court, near the northern end of the rupture, where en echelon fractures are observed in asphalt and right-lateral curb offsets of about 3 cm were recorded (stations 505–514, appendix 3, fig. 3.1).

Trace C

Trace C is the largest of the secondary ruptures produced by the South Napa earthquake. Tectonic rupture was documented over approximately 7 km, from about 1.5 km south of Old Sonoma Road to about 0.2 km north of Alston Park (figs. 1 and 9, appendix 4, figs. 4.1 to 4.3). A small amount of tectonic rupture on Trace C may have extended for an additional 1.1 km to the northwest based on UAVSAR data. Although ground cracks were observed along this lineament north of Alston Park, definitive tectonic faulting could not be demonstrated. From its northern terminus to Redwood Road, Trace C is within 150 m of a previously mapped Quaternary active fault (U.S. Geological Survey and California Geological Survey, 2006). South of Redwood Road, however, the rupture does not appear to be associated with any previously mapped fault traces.

The rupture is best expressed along its northern extent in Browns Valley, between Redwood Road and Browns Valley Road. Here, the rupture has a strike of 345° and it appears as fractures and buckles in asphalt, curbs, and sidewalks (stations 617–689, appendix 4, figs 4.2 and 4.3). Lateral offsets were observed primarily on paving stripes and curbs, and maximum strike-slip displacements of about 7 cm were observed between Browns Valley Road and Westminster Way (stations 623 and 677, appendix 4, figs. 4.2 and 4.3). Slip appears to decrease to the north to about 3 cm at Redwood Road (station 686, appendix 4, fig. 4.3).

North of Redwood Road, the strike of Trace C changes to approximately 335° and the rupture can only be seen intermittently in soil, where faulting is evidenced by short, en echelon fractures with little measurable displacement. Slip appears to increase near Alston Park, where en echelon fractures become more prominent and lateral offsets as great as 7 cm were recorded (stations 703–705, appendix 4, fig. 4.3). In this area, Trace C is less than 100 m east of Trace A and we speculate that the apparent slip increase may be a result of slip transfer from Trace A.

Farther north, beyond station 712 (appendix 4, fig. 4.3) to the end of the UAVSAR lineament, tension cracks were observed at several localities along the trend. However, there was no clear evidence for tectonic faulting, except possibly for observations of apparent left stepping cracks at stations 720–722 (appendix 4, fig. 4.3). No faulting was observed in a trench excavated across the lineament near these sites, however (Ryan Geological Consulting, 2015), so the origin of the UAVSAR lineament in this area is unclear.

South of Browns Valley Road, nearly 2 km of Trace C could not be accessed by field crews, but the rupture can be traced continuously south as a UAVSAR lineament (and seen intermittently in lidar imagery) to Thompson Road, where right lateral offsets of 3–5 cm were observed in pavement striping (stations 601–605, appendix 4, fig. 4.1). Comparable displacements were also recorded about 0.5 km to the south at Old Sonoma Road and Congress Valley Road (stations 577–591, appendix 4, fig. 4.1).

South of Old Sonoma Road, Trace C can be followed for an additional 1.5 km as discontinuous ground cracks and en echelon fractures, as the rupture gradually changes to a more northerly strike of 2°. Right-lateral slip measured along this reach of Trace C is quite small (~1 cm); rupture continuity must be inferred along this reach of Trace C, as slip is apparently too small to be observed in UAVSAR interferograms.

Trace D

As with Trace B, Trace D (fig. 1, appendix 5, fig. 5.1) was first identified from UAVSAR interferograms and then confirmed as a tectonic fault based on subsequent field investigations. This rupture strikes more westerly than other traces (~315°) and is less than 0.9 km long. Evidence for ground disturbance along the lineament are discontinuous cracks in pavement and driveways, damaged curbs, and tented and displaced sidewalk panels that may have resulted from block rotation. Observations of clear right-lateral faulting are lacking at most sites except for laterally displaced curbs of 3 cm or less at stations 768 and 781 (appendix 5, fig. 5.1).

Trace E

Trace E encompasses two disconnected linear segments that are located 300–400 m east of Trace C. The southernmost segment of rupture E is not visible in lidar or UAVSAR data; investigators were informed of this trace by landowners, and the rupture is inferred to be continuous between observations stations. The southernmost zone strikes 335° and extends for about 700 m, crossing Old Sonoma Road near its southern end where the rupture appears as a

distributed zone of parallel cracks that span the roadway, but with no measurable displacement (stations 785–786, appendix 6, fig. 6.1). North of Old Sonoma Road, right-lateral faulting is evidenced by left-stepping en echelon fractures that were observed in vineyards and dirt roadways. Strike-slip displacement is estimated to be 5 cm at station 790 (appendix 6, fig. 6.1).

The northern segment is visible in lidar and UAVSAR imagery, strikes approximately 315°, and is located about 0.5 km northwest of the northern end of the southern segment; it is unclear whether this segment might connect directly to the southern segment at the surface, or if the segments reflect a right-step. The northern zone is less than 200 m long, but faulting is clearly expressed by left-stepping en echelon fractures that trend up the side of a spur (stations 793–794, appendix 6, fig. 6.1). No lateral offsets were measured on this segment but are likely no more than a few centimeters.

Along trend with the northern segment, about 300 m to the northwest, more ground cracks are observed over an approximately 180-m-long zone that also strikes 315°. Cracks in this zone are described as small and discontinuous, with varying fracture orientations (mostly west trending). The origin of these fractures is unclear, and may therefore not be associated with the northern segment of Trace E.

Trace F

Trace F, located within the hills adjacent to the city of Napa, ruptured within about 100 m of previously mapped Quaternary-active traces of the West Napa Fault System (Helley and Herd, 1977; Bryant, 1982). Rupture is sinuous in this area, expressed as well-developed en echelon breaks with parallel fractures and short (10–50-m-long) branch faults. Overall, the rupture is located on the eastern slope of a small valley and strikes generally north–south, from its southern terminus north to about 90 m south of Old Sonoma Road (appendix 7, fig. 7.1) where the strike begins to rotate to a more northwesterly orientation (~325°). Measured displacements are right lateral and range from 4–5 cm (stations 806 and 816, appendix 7, fig. 7.1), with comparable vertical offsets that are up to the west, resulting in the formation of uphill facing scarps and a subtle side-hill bench. A trench excavated across the rupture near station 806 showed evidence for several prior Holocene earthquakes with vertical separations larger than what was produced in 2014, suggesting that prior earthquakes had produced significant, likely seismogenic, rupture on Trace F (Seitz and others, 2015; Ryan, 2014). It is therefore possible that Trace F may serve as a primary fault trace in future earthquakes on the West Napa Fault System.

UAVSAR data suggest that rupture on Trace F occurred along two disconnected segments north of Old Sonoma Road (appendix 7, fig. 7.1), where faulting appears as discontinuous, commonly sinuous fractures. Displacements are smaller than to the south (<3 cm; stations 826 and 831, appendix 7, fig. 7.1), but still display consistent, significant, west-up vertical offsets.

Trace G

Bryant (1982), identified an 8-km-long Holocene active trace of the West Napa Fault System that extends from American Canyon north to the Napa County Airport (fig. 1). From UAVSAR data, it appears that a small amount of coseismic fault slip occurred along nearly its entire length (Trace G). In addition, UAVSAR data indicate that Trace G ruptured to the northwest an additional 3 km from the airport to where Helley and Herd (1977) mapped several short fault traces (fig. 9).

Small ground cracks were observed along the fault trace in pavement at the Napa County Airport (stations 850–859, appendix 8, fig. 8.1), where a minor amount of distributed right-lateral deformation was observed in pavement striping (station 856, appendix 8, fig. 8.1). Except for a small ground fissure at station 860 (appendix 8, fig. 8.1), located north of the airport, no further field evidence of faulting or ground disturbance was observed along Trace G. Careful reconnaissance of curbs, streets, and railroad ties revealed no evidence of ground disturbance south of the airport.

From the UAVSAR data, it appears that Trace G ruptured over a length of more than 9.5 km. Slip on the Trace G rupture was most likely triggered by the South Napa earthquake and either did not reach the ground surface or was too small or distributed to produce visible evidence in the field.

Characteristics of Off-fault Ground Deformation

Overview

In addition to surface faulting produced by the South Napa earthquake, the event also caused widespread ground disturbance that was not along fault zones. This is true even though the earthquake produced only a limited amount of liquefaction and landslide-induced ground failure (Brocher and others, 2015). Of the more than 1,200 observation sites compiled for this report, more than 40 percent are not located anywhere near the tectonic fault traces (fig. 13). Of these anomalous sites, less than 20 percent of the stations had deformation that could readily be attributed to seismically induced, shallow slope failure (for example, slumps, soil and rock falls) or to lateral spreading from liquefaction or soft clay failure. The remaining sites of ground deformation cannot be readily attributed to either shaking-induced ground failure or faulting and have been classified as being of uncertain origin. Some of these features may be indicative of faulting or bedrock control and are located along UAVSAR lineaments, whereas others have no mappable extent. Observations for these features are organized in the appendixes by geographic regions that isolate sites with similar ground deformation characteristics (fig. 13).

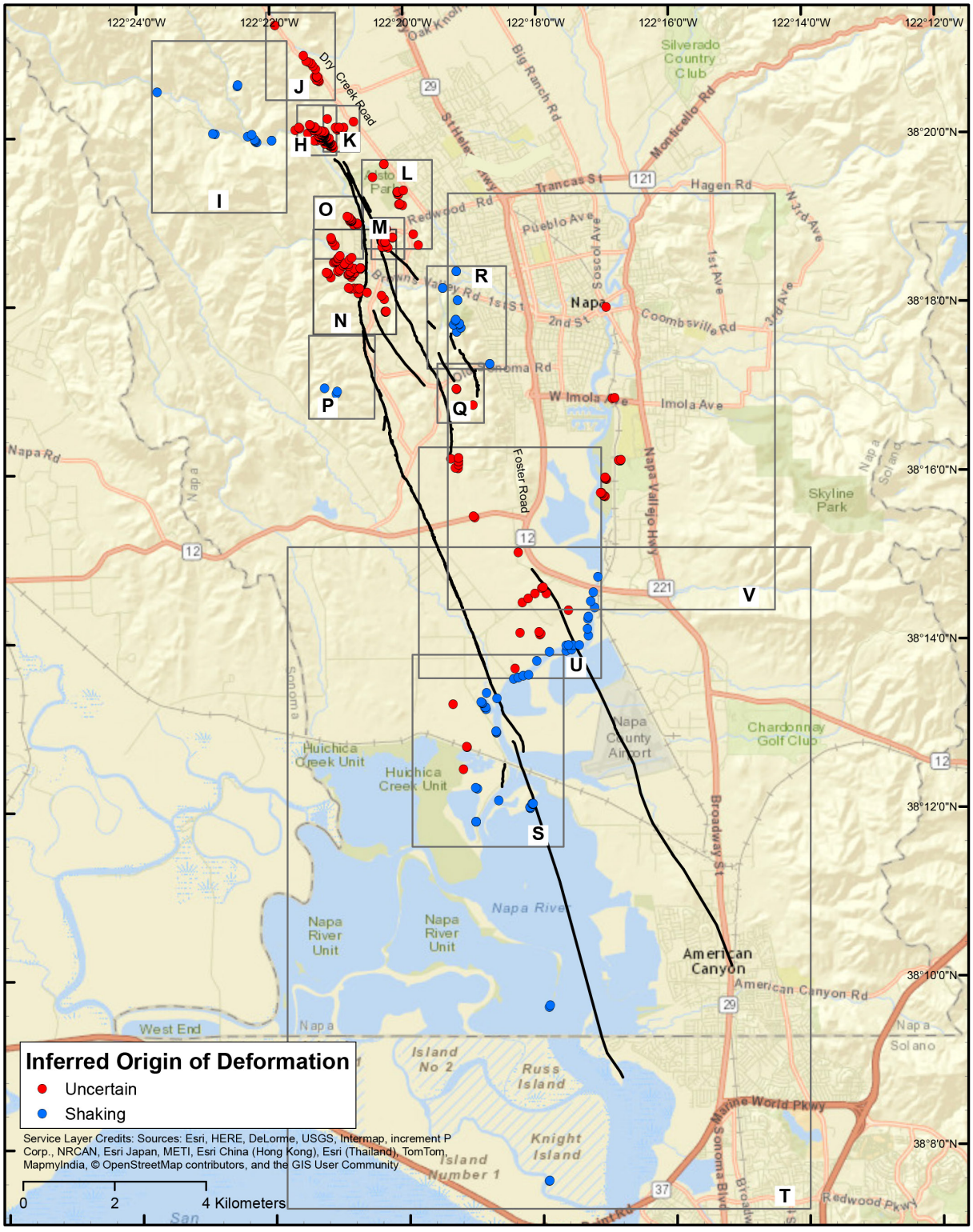

Figure 13. Map showing locations of ground deformation produced by the August 24, 2014, South Napa earthquake that are not located on known tectonic fault traces (black lines). Blue circles, deformation clearly related to lateral spreading or shallow slope failure; red circles, origin of deformation is uncertain; H–V, regions (rectangles).

Summary Descriptions

Shaking-induced Deformation Owing to Landslide Reactivation or Fill Settlement (Regions I, P, R; Appendix 9)

Many observations of ground disturbance can readily be attributed to shallow soil movement owing to shaking, because of either landslide reactivation or settlement of road fill, and are classified as being of shaking origin. One area where such features are common is in Region R (fig. 13), near a ridge on the west side of the Napa Valley, east of Thompson Road and south of Browns Valley Road (stations 1039–1045, appendix 9, fig. 9.3). These locations contain open fractures that are associated with sinuous, roughly slope-parallel, northeast-trending lineaments that appear in UAVSAR interferograms. Most of these sites and lineaments are found within a previously mapped landslide (Wagner and Gutierrez, 2010); the character of these fractures and lineaments is consistent with reactivation of the slide mass during the earthquake.

In Region I (fig. 13), there are several observations of cracks and dips in pavement, and damage to a bridge approach on Redwood Road in the hills west of Trace A (stations 1146–1156, appendix 9, fig. 9.1). The nature of these features is indicative of shaking-induced settlement of the road bed. A large fissure observed across a dirt road and nearby compressional features located about 1 km north of the intersection of Redwood Road and Mt. Veeder Road (stations 1157–1158, appendix 9, fig. 9.2) are found within a previously mapped landslide (Wagner and Gutierrez, 2010) and are likely due to reactivation of a portion of the slide mass during the earthquake.

Similarly, minor cracking associated with previously mapped landslides about 1 km west of Trace A and 3 km north of State Route 12/121 (Region P, fig. 13) are also likely due to shaking.

Shaking-Related Features Resulting from Lateral Spreads and Bank Failures (Regions S, T; Appendix 10)

Numerous sites of failures along banks of the Napa River are documented in Region T (fig. 13). Bank failures have been identified from as far south as Knight Island (stations 1087–1088, appendix 10, fig. 10.2) north to Officer George F. Butler Bridge on State Route 12/29 (station 1110, appendix 10, fig. 10.2). These are mostly isolated, small-scale features, although there are areas of concentrated bank slumps, most notably soil slumps near where Trace G crosses the Napa River (stations 1097–1102, appendix 10, fig. 10.2).

Fissures in natural soil and pavement located on Green Island and near the west bank of the Napa River between Green Island and Bull Island (Region S, fig. 13) may be attributable to shallow lateral spreading toward a free face. At these locations, there are reports of extensional fractures striking near parallel to the shoreline, although no observations of sand boils or vented materials were noted. On Green Island, several observations are located close to Trace A and suggest right-lateral motion (stations 1060 and 1064, appendix 10, fig 10.1) that may be related to faulting, but overall, these features are consistent with lateral spreads. Several stations in this region west of the Napa River (stations 1069–1072, 1080, appendix 10, fig. 10.1) appear to be related to lateral-spread failure owing to settlement of filled railroad and road beds.

Ridgetop Fractures (Regions H, K; Appendix 11)

Initial reconnaissance in Region H identified a zone of large, open fissures more than 700 m long by about 100 m wide concentrated near the top of a northwest-trending ridge (appendix 11, fig 11.1). Displacement vectors indicated that fracture opening was generally normal to the overall ridgetop trend, consistent with downslope movement. In addition, several localities in the valley floor near Redwood Creek showed evidence for southwest-northeast directed compression (for example, stations 906 and 990, appendix 11, fig. 11.1). In Region K, about 500 m to the east, a single, linear, ridge-parallel fissure, nearly 70 m long, was discovered on a ridge crest and associated with several small ground cracks nearby (stations 1176–1186, appendix 11, fig. 11.2).

Mapping of the ground fissures in Region H document several parallel sets of fractures that are generally oriented approximately 30° clockwise with respect to the overall ridge crest strike (~305°). This produces a left-stepping pattern of fractures within the overall zone. Moreover, most of the fractures are bounded between two UAVSAR lineaments, with the northeast boundary being the Trace C lineament. Displacement on the fissures generally is oriented normal to the ridge crest strike, which produces an apparent left-lateral sense of motion across many of the fractures.

The geometry and displacement sense of the fissures could be explained by clockwise block rotation within a right-lateral shear zone bounded by the UAVSAR lineaments. Subsequent consultant trenches across several of the fissures showed that the they are concentrated in areas where the underlying bedrock was a steeply dipping shale (Ryan Geological Consulting, 2015). Fractures are coincident with bedding planes and die out with depth. These observations are consistent with ridge spreading as the dominant mechanism for producing the features (Ponti and Wells, 1991). In addition, no shearing or evidence of a substantial fault was observed in bedrock exposed in trenches that crossed the UAVSAR lineament that appears connected to Trace C to the south (Ryan Geological Consulting, 2015).

These ridgetop fractures are likely caused by shaking-induced ridgetop spreading or deep-seated failures along bedding planes. If any tectonic signal associated with the UAVSAR lineaments are present, it is likely very minor and not a causative factor for the observed ground deformation features.

Isolated Cracking on Slopes (Regions J, Q; Appendix 12)

Numerous cracks in pavement and soil were identified along the range front west of Dry Creek Road, about 2.5 to 5 km north of Redwood Road (Region J, fig. 13). One area of concentrated linear cracks that display both extensional and compressive deformation in soil and pavement (stations 1159–1168, appendix 12, fig. 12.1) is associated with a previously mapped landslide (Wagner and Gutierrez, 2010). Ground cracks in Region J are likely shaking related, associated with slide reactivation, pavement lurching, decoupling, or settlement of road fill. These sites are directly north of the rupture and likely experienced especially strong ground motions because of rupture directivity (Baltay and Boatwright, 2015).

Very minor cracks were also identified on vineyard slopes about 0.2–0.7 km southeast of Old Sonoma Road, approximately on trend with the southern terminus of Trace E (Region Q, fig. 13). These are all open, isolated fractures that are less than a few meters long. Station 1034 (appendix 12, fig. 12.2) is located adjacent to a previously mapped landslide (Wagner and Gutierrez, 2010). These features are likely due to shaking and minor downslope movement.

Fractures Associated with UAVSAR Lineaments (Regions L, O, R, U; Appendix 13)

UAVSAR interferograms reveal several northwest-trending lineaments that indicate the presence of differential ground movement likely associated with faults or other large-scale geologic structures. In several locations, there is no documented evidence for surface disturbance along these trends. In other cases, observed ground deformation was minor and lacked consistent patterns or displacement that would suggest tectonic faulting. Along the range front on the west side of the Napa Valley, UAVSAR data reveal three lineaments that appear to be associated with previously mapped faults of the West Napa Fault System (Bryant, 1982; Wesling and Hanson, 2008; Helley and Herd, 1977; fig. 9). These include an approximately 0.8-km-long lineament west of Dry Creek Road near Alston Park (Region L, fig. 13), an approximately 1-km-long lineament north of Browns Valley Road (Region R, fig. 13), and an approximately 1-km-long lineament located between Foster Road and State Route 29, about 1 km north of State Route 12/121 (Region U, fig. 13; appendix 13, fig. 13.4). Although not associated with a previously mapped fault, another set of lineaments in Region U can be inferred from the UAVSAR data to connect and form a single approximately 3-km-long northwest-trending zone that starts from near the southern terminus of Trace C (near station 1128, appendix 13, fig 13.4) and extends to about 0.6 km west of the northern terminus of Trace G (station 1118, appendix 13, fig 13.4). If this interpretation is correct, this structure may represent the southern extension of Trace C and possible linkage across a left step to Trace G. The presence of Home Hill (appendix 13, fig 13.4) in the stepover between these two lineaments is consistent with such a linkage.

No evidence for surface disturbance was found to be associated with the lineament near Foster Road; therefore, movement along this zone was likely small, distributed over a wide enough area to avoid detection, and (or) did not fully reach the surface. A very small pavement crack with the west side up and only 0.1 cm of apparent right-lateral offset (station 1048, appendix 13, fig 13.3), is the only observation of ground disturbance associated with the lineament in Region R. Near Alston Park, there were many observations of short, hairline fractures in both soil and pavement with no visible displacement or lineament-parallel, en echelon pattern of fractures (stations 1191–1200, appendix 13, fig 13.1). For the lineament extending south from Trace C, hairline cracks are observed in pavement and soil at State Route 12/121 (stations 1125–1126, appendix 13, fig. 13.4) and at Stanly Cross Road (station 1118, appendix 13, fig. 13.4). These are the only sites of documented surface disturbance anywhere along this trend.

It is compelling to consider that these UAVSAR lineaments identify parts of other active fault traces triggered by the South Napa earthquake. However, this cannot be demonstrated by the surface observations alone, and there may be other possible explanations for these lineaments that better fit the surface data. A horizontal-displacement profile constructed from UAVSAR data across the Alston Park lineament in Region L (DeLong and others, 2016) provides only ambiguous evidence for tectonic movement and suggests that much of the movement may be vertical. This raises the possibility that lineaments along the range front (and potentially others) could be produced by shaking-related settlement along a fault-bounded bedrock–basin contact, or a contact between sedimentary units with different geotechnical properties. Differential movement could also be enhanced if these zones serve as wave guides. In any event, it remains unresolved whether these lineaments delineate potentially active faults that could pose a significant surface-rupture hazard in the future or inactive structures or contacts.

Additional lineaments are identified from UAVSAR data west of Trace A near Browns Valley (Region O, fig. 13). An approximately 400-m-long lineament strikes at about 330° and

crosses Partrick Road at an oblique angle where well-expressed ground cracks, with predominantly horizontal opening both in pavement and soil, are evident (stations 1285–1290, appendix 13, fig. 13.2). The fracture patterns and displacements are not indicative of faulting. However, this lineament is on trend with a short, faint lineament 0.9 km to the southeast that appears to branch from Trace A at the location where afterslip ceases. Several observers have speculated that this lineament was produced by shaking that caused lateral movement toward a creek located 130–160 m to the south of Partrick Road. If this were true, however, one might expect the rupture to parallel the terrace riser edge more closely, which it does not.

A second approximately 220-m-long lineament with average strike of about 330° is associated with notable tension cracks near Montana Drive (appendix 13, fig. 13.2). Cracks strike approximately parallel to the lineament and trend uphill along the northeast side of a spur. Displacement sense is dominantly extensional, although one observer noted about 2 cm of right-lateral displacement at one site (station 1305, appendix 13, fig. 13.2).

The origin of these features west of Trace A remains enigmatic. Although disconnected from Trace A, both the Montana Drive and Partrick Road lineaments potentially define faults that branch to the northwest from Trace A in Browns Valley and could consume a small amount of slip near the northern end of the rupture. However, if these lineaments are tectonic, observed ground fractures do not demonstrate a consistent displacement sense that would support dextral faulting. The topographic setting and character of the Montana Drive fractures are also somewhat similar to those seen on ridgetops in Region H and could be of similar origin.

Areas of Extensive Curb and Sidewalk Damage (Regions M, N; Appendix 14)

In addition to damage from fault rupture along traces A and C, the Browns Valley area also experienced extensive damage to concrete curbs and sidewalks located hundreds of meters away from the rupture. While these types of features were observed locally throughout the region, damage was especially concentrated in the following locations in Browns Valley: (1) the large housing subdivision located west of Trace A and south of Partrick Road (Region N) and (2) the vicinity of Westminster Way about 100 m east of Trace C and 100–200 m northwest of the northern terminus of Trace D (Region M).

In these areas, most of the damage noted appears to be a result of compressive forces—tented and heaved sidewalks, overlapping and overturned sidewalk panels, and crushed or "exploded" curbs. Cohen-Waeber and others (2014) however, have noted that extensional cracks and pull aparts in sidewalks and curbs are in fact more common than compressional features but not as prominent and therefore tend not to be noted by observers. In fact, comparable damage to adjacent pavement or soil was rare, which would argue against significant localized ground deformation. Thus, this type of curb and sidewalk damage in general is most likely driven by dynamic shaking and decoupling of the brittle concrete from the natural ground and not by permanent ground deformation in a notable way.

In Region N, compressive curb and sidewalk damage is common west of Trace A and virtually nonexistent to the east (appendix 14, fig 14.2). Furthermore, northeast-trending roads (for example, Morningside Drive) appear to have sustained more damage than those trending southeast. The northeast -trending roads are oriented 30°–45° clockwise relative to Trace A and thus are well aligned in the direction of the principal compressive stress field for a north-trending fault zone, consistent with the compressive deformation observed.

This area was not systematically studied by observers, but these general observations appear to be supported by Cohen-Waeber and others' (2014) detailed evaluation of sidewalk

extension and compression over a part of Region N. Northeast-trending streets in this region west of Trace A experienced net shortening on the order of about 0.02 percent, whereas southeast-trending streets extended by 0.015 percent (Cohen-Waeber and others, 2014). Moreover, both northeast- and southeast-trending streets east of Trace A experienced no net strain at all. There appears to be an association, therefore, between the distribution of sidewalk and curb damage and permanent ground deformation, and thus the area of Region N west of Trace A may have been impacted by distributed dextral shearing over a broad area. Coupled with the changes in strike to Trace A in this area and cessation of afterslip, the distribution of curb and sidewalk damage is further evidence for broadly distributed deformation in this region of the fault zone.

Pavement Cracks South of the Soda Creek Fault, City of Napa (Region V; Appendix 15)

Following release of the Cosmo-Skymed InSAR data on August 27, 2014, investigators noticed an alignment of fringe perturbations along a north-northeast trend through the City of Napa near the Napa River, extending from about 1 km south of the southern terminus of the Soda Creek fault (fig. 9) south to Kennedy Park (near station 1320, appendix 15, fig. 15.1). Observations of ground deformation along this trend are limited to intermittent, very minor cracking in pavement. The most notable features were damage to the south abutment of the Soscol Avenue Bridge, with compression consistent with clockwise rotation of the bridge deck (station 1341, appendix 15, fig. 15.1), and extensional cracking in the abutment of a bridge on Imola Avenue (station 1339, appendix 15, fig. 15.1). Most of the pavement cracks are concentrated in Kennedy Park in close proximity to the bank of the Napa River.

It is unclear what the specific cause of the fringe perturbations in the satellite InSAR might be. The proximity of most ground cracks and bridge damage to the Napa River implicates lateral spread failure as a likely cause for these features.

Conclusions

The large extent of surface faulting and other ground deformation from the August 24, 2014, South Napa earthquake triggered an intensive response by numerous geologists to document the prevalence and kinematics of ground deformation through field-based ground observations. Observations, photographs, and field maps collected as part of the response were integrated with interpretations of high-resolution aerial photography, airborne lidar, and InSAR to produce a digital map of fault rupture and linear zones of ground deformation.

The results of this compilation reveal that faulting occurred within a 2-km-wide zone on six roughly parallel traces within the West Napa Fault System (fig. 1). Most fault slip and all afterslip occurred on the westernmost trace (A), where rupture could be traced for more than 21 km. Maximum coseismic slip was greater than 40 cm and possibly as great as 60 cm, with the slip maximum located about 10 km north of the epicenter. Widely distributed faulting and ground deformation, coupled with UAVSAR data, suggest that the northern end of the Trace A rupture may be significantly affected by complex subsurface structure.

UAVSAR interferograms were particularly invaluable for identifying and mapping secondary traces with small displacements and for delineating overall details of the rupture pattern, especially where slip was small or not observable in the field. Because evidence for fault rupture on the secondary traces was discontinuous, UAVSAR data helped confirm continuity of deformation and showed that rupture extended beyond where it could be mapped using imagery

or lidar. UAVSAR data also highlighted other possible zones of fault rupture, several of which are coincident with previously mapped fault traces. UAVSAR lineaments may highlight traces of active faults that could produce significant surface rupture in future earthquakes. However, clear evidence for faulting is confirmed on only two such lineaments (Traces B and D). Additional evaluation throughout the region is recommended to determine whether structures along additional UAVSAR lineaments are active faults or possible structural boundaries where shaking may produce small differential displacements.

The South Napa earthquake response represents one of the first times when most reconnaissance data were collected and disseminated electronically. This lead to a substantial volume of data that was collected and distributed rapidly. However, the volume of information and lack of standards for data collection and dissemination present new challenges to large-scale compilation efforts. To take full advantage of new technology, geologists must develop more uniform data collection and dissemination processes and guidelines and work toward standardizing field observations and reporting formats. An important lesson learned is the need to set standards for the minimum amount of information that should be collected during post-earthquake geologic reconnaissance. From our experience with the South Napa earthquake post-earthquake investigation, we recommend the following as a starting point:

1. For every observation made, the following information should be recorded:
   A. Date and time of observation (with specified time zone) including times of measurements and photographs.
   B. Method used for determining location, including equipment used, map scale, image resolution, and GPS parameters, where applicable. Locations should be verified against high-quality base maps or imagery before dissemination.
   C. Names and affiliations of all field team personnel.
   D. Verified location, corrected as necessary before dissemination.
   E. For photographs, in addition to location, time, and camera metadata, look direction and estimated distance to the feature of interest. Photographs should also include a scale if documenting feature displacements.
   F. Types of equipment used for measuring lengths, azimuths and angles
2. When slip measurements are taken, the following information should be recorded:
   A. Type of offset feature where measurement is made (for example, soil, curb, fence)
   B. Width of the deformation zone over which slip is measured and whether the measurement represents minimum slip or not.
   C. Azimuth of the fault trace. If the zone consists of en echelon fractures, measurement should be of the zone azimuth, not the fracture azimuth.
   D. Where piercing points are clearly identified, the azimuth, plunge angle, and length of the slip vector, or as many components of the slip vector as can be measured (for example, horizontal, vertical, fault normal) as well as displacement sense.
   E. Where piercing points are not well defined, separation (measured normal to the offset feature), and azimuth of the offset feature.
3. In addition, it is important to include observations for locations where deformation was anticipated but not observed, such as along projected fault strike or where InSAR data indicate the presence of localized surface deformation.

The South Napa earthquake post-earthquake investigation was an excellent test bed for applying new technology to improve post-earthquake field response. The immense amount of

field data collected and integrated in studying this earthquake provides a rich foundation for future research. This earthquake highlighted active fault traces not previously recognized and identified zones that could possibly produce significant rupture in future events. The event has also highlighted possible structural complexities at the northern end of the rupture zone that poses questions for how slip on the West Napa Fault System propagates to the north. Answering these new questions requires ongoing geologic and geophysical investigations and continued development of new methods for identifying and characterizing seismogenic structures, in addition to documenting the effects from future earthquakes.

Acknowledgments

We thank the following landowners and property managers for allowing us access to perform the field work necessary to produce this report: Julie Arbuckle, Gustavo Avina, Michael Beaulac, Zach Berkowitz, Armando Ceja, Pablo Ceja, Robert DeLeuze, Rob and Kristan Forloine, David Graves, Chris Gurney, Toby Hallkovich, Michael Hendry, Maxine Jacobs, Steven Moulds, Theo Perez, Tony Trouchard, Al Wagner, Dana Zaccone, and Debby Zygielbaum. We thank Martin Pehl, Airport Manager, County of Napa, for allowing access to their active runways to examine and map the fault rupture on Trace G. We thank Andrea Donnelan and the UAVSAR project team at NASA's Jet Propulsion Laboratory (JPL) for providing interferogram data, analyses tools, and assistance in interpretation. Finally, we wish to thank Josh Livni, of Google Inc., for providing access to high-resolution image tiles from Google's August 24, 2014, post-earthquake aerial reconnaissance under the Creative Commons CC BY 4.0 license. Helpful reviews by by Katherine Scharer, Katherine Kendrick, and all contributors to this effort greatly improved this product.

References Cited

Beyzaei, C., Shriro, M., and Bray, J., 2014, Performance of ground and buried utilities, section 6 *in* Bray, J., Cohen-Waeber, J., Dawson, T., Kishida, T., and Sitar, N., eds., Geotechnical Engineering Reconnaissance of the August 24, 2014 M6 South Napa earthquake: Geotechnical Extreme Events Reconnaissance Association Report GEER-037.

Baltay, A.S., and Boatwright, J., 2015, Ground-motion observations of the 2014 South Napa Earthquake: Seismological Research Letters, v. 86, no. 2A, p. 355–360, doi:10.1785/0220140232.

Bray, J., Cohen-Waeber, J., Dawson, T., Kishida, T., and Sitar, N., eds., 2014, Geotechnical Engineering Reconnaissance of the August 24, 2014 M6 South Napa earthquake: Geotechnical Extreme Events Reconnaissance Association Report GEER-037, 415 p., accessed February 2015 at http://www.geerassociation.org/component/geer_reports/?view=geerreports%20&id=29&layout=default.

Brocher, T.M., Baltay, A.S., Hardebeck, J.L., Pollitz, F.F., Murray, J.R., Llenos, A.L., Schwartz, D.P., Blair, J.L., Ponti, D.J., Lienkaemper, J.J., Langenheim, V.E., Dawson, T.E., Hudnut, K.W., Shelly, D.R., Dreger, D.S., Boatwright, J., Aagaard, B.T., Wald, D.J., Allen, R.M., Barnhart, W.D., Knudsen, K.L., Brooks, B.A., and Scharer, K.M., 2015, The M_w 6.0 24 August 2014 South Napa Earthquake: Seismological Research Letters, v. 86, no. 2A, p. 309–326, https://doi.org/10.1785/0220150004.

Brooks, B.A., Minson, S.E., Glennie, C.L., Murray, J.R., Hudnut, K.W., Ericksen, T., Langenheim, V.E., Lockner, D.A., Dawson, T.E., and Lutz, A.T., 2015, Uncorking shallow slip and the slip history of the 2014 South Napa earthquake [abs.]:, American Geophysical Union, Fall Meeting 2015 Abstracts, abstract no. G21C-04, available at http://abstractsearch.agu.org/meetings/2015/FM/G21C-04.html.

Bryant, W.A., 1982, West Napa fault zone; Soda Creek fault (East Napa fault): California Division of Mines and Geology Fault Evaluation Report FER-129, 9 p.

California Earthquake Clearinghouse, 2009, California Post-Earthquake Clearinghouse Draft Operational Plan: California Earthquake Clearinghouse, 22 p., accessed February 2016 at http://www.californiaeqclearinghouse.org/wp-content/uploads/2009/06/chplan090324.pdf.

Clahan, K. B., Wesling, J. R., and Brossy, C., 2011, Paleoearthquake chronology along the northern West Napa Fault Zone, Napa County, California: Final Technical Report for the U.S. Geological Survey National Earthquake Hazards Reduction Program, Award no. 07HQGR0081.

Cohen-Waeber, J. Lanzafame, R., and Bray, J., 2014, Effects of surface fault rupture on infrastructure, section 5 *in* Bray, J., Cohen-Waeber, J., Dawson, T., Kishida, T., and Sitar, N., eds., Geotechnical Engineering Reconnaissance of the August 24, 2014 M6 South Napa earthquake: Geotechnical Extreme Events Reconnaissance Association Report GEER-037.

Dawson, T., Kelson, K., Wesling, J., Hudnut, K. and Ponti, D., 2014, Surface fault rupture associated with the M 6.0 South Napa earthquake of August 24, 2014, section 3 *in* Bray, J., Cohen-Waeber, J., Dawson, T., Kishida, T., and Sitar, N., eds., Geotechnical Engineering Reconnaissance of the August 24, 2014 M6 South Napa earthquake: Geotechnical Extreme Events Reconnaissance Association Report GEER-037.

DeLong, S.B., Donnellan, A., Ponti, D.J., Rubin, R.S., Lienkaemper, J.J., Prentice, C.S., Dawson, T.E., Seitz, G., Schwartz, D.P., Hudnut, K.W., Rosa, C.M., Pickering, A., and Parker, J.W., 2016, Tearing the terroir—Details and implications of surface rupture and deformation

from the 24 August 2014 M6.0 South Napa earthquake, California: Earth and Space Science, v. 3, no. 10, p. 416–430, http://doi.org/10.1002/2016EA000176.
Donnellan, A., Parker, J., Hensley, S., Pierce, M., Wang, J., and Rundle, J., 2014, UAVSAR observations of triggered slip on the Imperial, Superstition Hills, and East Elmore Ranch Faults associated with the 2010 *M*7.2 El Mayor-Cucapah Earthquake: Geochemistry, Geophysics, Geosystems, v. 15, no. 3, p. 815–829, https://doi.org/10.1002/2013GC005120.
Dreger, D., Huang, M., Rodgers, A., Taira, T., and Wooddell, K., 2015, Kinematic Finite-Source Model for the 24 August 2014 South Napa, California, Earthquake from Joint Inversion of Seismic, GPS, and InSAR Data: Seismological Research Letters, v. 86, no. 2, p. 327–334.
Earthquake Engineering Research Institute, 1996, Post-Earthquake Investigation Field Guide—Learning from Earthquakes: Oakland, Calif., Earthquake Engineering Research Institute, 196 p.
European Space Agency, 2015, Sentinel 1A data: European Space Agency, INSARAP Project, SEOM Study. [Interferogram accessed November 2015 at http://insarap.org/napa.html.]
Field, E., Arrowsmith, R., Biasi, G., Bird, P., Dawson, T., Felzer, K., Jackson, D., Johnson, K., Jordan, T., Madden, C., Michael, A., Milner, K., Page, M., Parsons, T., Powers, P., Shaw, B., Thatcher, W., Weldon, R., and Zeng, Y., 2014, Uniform California Earthquake Rupture Forecast, Version 3 (UCERF3)—The Time-Independent Model: Bulletin of the Seismological Society of America, v. 104, no. 3, p. 1122–1180, https://doi.org/10.1785/0120130164.
Floyd, M.A., Walters, R.J., Elliott, J.R., Funning, G.R., Svarc, J.L., Murray, J.R., Hooper, A.J., Larsen, Y., Marinkovic, P., Burgmann, R., Johanson, I.A., and Wright, T.J., 2016, Spatial variations in fault friction related to lithology from rupture and afterslip of the 2014 South Napa, California, earthquake: Geophysical Research Letters, v. 43, no. 13, p. 6808–6816, https://doi.org/10.1002/2016GL069428.
Galehouse, J.S. and Lienkaemper, J.J., 2003, Inferences drawn from two decades of alinement array measurements of creep on faults in the San Francisco Bay Region: Bulletin of the Seismological Society of America. v. 93, no. 6, p. 2415–2433
Hardebeck, J.L., and Shelly, D.R., 2016, Aftershocks of the 2014 South Napa, California, Earthquake—complex faulting on secondary faults: Bulletin of the Seismological Society of America, v. 106, no. 3, p. 1100–1109, https://doi.org/10.1785/0120150169.
Harder, L., 2014, Performance of Dams and Levees, section 7 *in* Bray, J., Cohen-Waeber, J., Dawson, T., Kishida, T., and Sitar, N., eds., Geotechnical Engineering Reconnaissance of the August 24, 2014 M6 South Napa earthquake: Geotechnical Extreme Events Reconnaissance Association Report GEER-037.
Helley, E.J., and Herd, D.G., 1977, Map showing faults with Quaternary displacement, northeastern San Francisco Bay Region, California: U.S. Geological Survey Miscellaneous Field Studies Map MF-881, scale 1:125000.
Hudnut, K.W., Brocher, T.M., Prentice, C.S., Boatwright, J., Brooks, B.A., Aagaard, B.T., Blair, J.L., Fletcher, J.B., Erdem, J.E., Wicks, C.W., Murray, J.R., Pollitz, F.F., Langbein, J., Svarc, J., Schwartz, D.P., Ponti, D.J., Hecker, S., DeLong, S., Rosa, C., Jones, B., Lamb, R., Rosinski, A., McCrink, T.P., Dawson, T.E., Seitz, G., Glennie, C., Hauser, D., Ericksen, T., Mardock, D., Hoirup, D.F., Bray, J.D., and Rubin, R.S., 2014, Key recovery factors for the August 24, 2014, South Napa earthquake: U.S. Geological Survey Open-File Report 2014–1249, 51 p., https://doi.org/10.3133/ofr20141249.

Jones, T.W., Marzen, L., and Chappelka, A., 2015, Horizontal accuracy assessment of Global Positioning System data from common smartphones: Papers in Applied Geography, v. 1, no. 1, p. 59–64, https://doi.org/10.1080/23754931.2015.1009304.

Lienkaemper, J.J., DeLong, S.B., Domrose, C.J., and Rosa, C.M., 2016, Afterslip behavior following the *M*6.0, 2014 South Napa earthquake with implications for afterslip forecasting on other seismogenic faults: Seismological Research Letters, v. 87, no. 3, p. 609–619, https://doi.org/10.1785/0220150262.

Morelan, A., Trexler, C., and Oskin, M., 2015, Surface-rupture and slip observations on the day of the 24 August 2014 South Napa earthquake: Seismological Research Letters, v. 86, no. 4, p. 1119–1127. [Supplemental materials also available online at https://ucdavis.app.box.com/s/9zsz84638fp90grhikzx.]

NASA, 2014, M6.0 South Napa Earthquake, August 24, 2014: Jet Propulsion Laboratory, Advanced Rapid Imaging and Analysis (ARIA) Center for Natural Hazards, accessed October 2015 at https://aria.jpl.nasa.gov/node/39.

NASA, 2015, UAVSAR data [line names SanAnd_05510, SanAnd_05512, and SanAnd_23511; InSAR Pair processing mode; date range Nov. 5, 2012 to Aug. 29, 2014]: NASA, Jet Propulsion Laboratory database, accessed October 2015 at http://uavsar.jpl.nasa.gov/cgi-bin/data.pl.

Ponti, D.J., and Wells, R.E., 1991, Off-fault ground ruptures in the Santa Cruz Mountains, California—Ridge-top spreading versus tectonic extension during the 1989 Loma Prieta earthquake: Bulletin of the Seismological Society of America, v. 81 no. 5, p. 1480–1510.

Ponti, D.J., Rosa, C.M., and Blair, J.L., 2019, Digital datasets documenting fault rupture and ground deformation features produced by the Mw 6.0 South Napa Earthquake of August 24, 2014: U.S. Geological Survey Data Release, https://doi.org/10.5066/F7P26W84.

Rosen, P.A., Hensley, S., Joughin, I.R., Li, F.K., Madsen, S.N., Rodríguez, E., and Goldstein, R.M., 2000, Synthetic Aperture Radar Interferometry: Proceedings of the IEEE, v. 88, no. 3, p. 333–382.

Rosen, P.A., Hensley, S., Wheeler, K., Sadowy, G., Miller, T., Shaffer, S., Muellerschoen, R., Jones, C., Zebker, H., and Madsen S., 2006, UAVSAR—A new NASA airborne SAR system for science and technology research [abs.]: 2006 IEEE Conference on Radar, p. 8, https://doi.org/10.1109/RADAR.2006.1631770.

Rosinski, A., Ortiz, M., Tremayne, H., Blair, L., and Julius, A., 2015, California Earthquake Clearinghouse After-Action Report—South Napa Earthquake: California Earthquake Clearinghouse, 35 p., accessed March 2016 at http://www.californiaeqclearinghouse.org/wp-content/uploads/2014/08/California_Earthquake_Clearinghouse_After_Action_Report-South_Napa_Earthquake-2015.04.17.pdf.

Rubin, R.S., Dawson, T.E., and Mareschal, M., 2014, Pre-earthquake paleoseismic trenching in 2014 along a mapped trace of the West Napa fault [abs.]: American Geophysical Union, Fall Meeting 2014 Abstracts, abstract no. S33F-4934, available at http://abstractsearch.agu.org/meetings/2014/FM/S33F-4934.html.

Ryan Geological Consulting, 2015, Fault Investigation Report, Anthem Winery and Vineyards, LLC, 3454 Redwood Road, Napa, California: Orinda, Calif., Ryan Geological Consulting, job no. 1210.100.

Ryan, K., 2014, Fault Setback Map, Napa Oaks, Old Sonoma Road and Casswall Street Napa, California, For Davidson Homes: prepared for Berlogar Stevens and Associates, job no. 3280.002.

Seitz, G., Ryan, K., and Rosa, C., 2015, Multiple Holocene-age events on the easternmost surface rupture of the August 24, 2014 South Napa Earthquake [abs.]: Seismological Research Letters, v. 86, no. 2B, p. 634, https://doi.org/10.1785/0220150017.

U.S. Geological Survey and California Geological Survey, 2006, Quaternary fault and fold database of the United States: U.S. Geological Survey database, accessed July 31, 2015, at https://earthquake.usgs.gov/hazards/qfaults/.

Wagner, D.L., and Gutierrez, C.I., 2010, Geologic map of the Napa 30' by 60' quadrangle, California: California Geological Survey, scale: 1:1,00,000.

Wagner, N., Luque, R., Sitar, N., Ground deformation in the very near fault region, section 5 *in* Bray, J., Cohen-Waeber, J., Dawson, T., Kishida, T., and Sitar, N., eds., Geotechnical Engineering Reconnaissance of the August 24, 2014 M6 South Napa earthquake: Geotechnical Extreme Events Reconnaissance Association Report GEER-037.

Wei, S., Barbot, S., Graves, R., Lienkaemper, J., Wang, T., Hudnut, K., Fu, Y., and Helmberger, D., 2015, The 2014 M_w 6.1 South Napa Earthquake—A Unilateral Rupture with Shallow Asperity and Rapid Afterslip: Seismological Research Letters, v. 86, no. 2A, p. 344–354, https://doi.org/10.1785/0220140249.

Wesling, J.R., and Hanson, K.L., 2008, Mapping of the West Napa Fault Zone for input into the northern California Quaternary fault database: Final Technical Report for U.S. Geological Survey External Award no. 05HQAG0002.

Zandbergen, P.A., 2009, Accuracy of iPhone locations—A comparison of assisted GPS, WiFi and cellular positioning: Transactions in GIS, v. 13, no. s1, p. 5–25, https://doi.org/10.1111/j.1467-9671.2009.01152.x

Glossary

CalOES California Office of Emergency Services
CGS California Geological Survey
DEM digital elevation model
DWR California Department of Water Resources
GPS Global Positioning System
EXIF Exchangeable image file format, a standard that specifies the formats for images, sound, and ancillary tags used by digital cameras or other systems handling image and sound files
GDOP geometric dilution of precision
GEER Geotechnical Extreme Events Reconnaissance
HDDS Hazards Data Distribution System
InSAR interferometric synthetic aperture radar
lidar light detection and ranging
PEER Pacific Earthquake Engineering Research Center
SAR synthetic aperture radar
SNE South Napa earthquake of August 24, 2014
UAVSAR uninhabited aerial vehicle synthetic aperture radar
USGS U.S. Geological Survey
WNFS West Napa Fault System

Appendix 1. Tabulated Observations and Photographs of Surface Faulting and Ground Deformation Produced by the M_w 6.0 South Napa Earthquake of August 24, 2014—Explanation

Introduction

Appendixes 2 through 15 contain maps and a table of tabulated descriptions, slip measurements, and photographs of surface faulting and ground deformation features produced by the M_w 6.0 South Napa Earthquake on August 24, 2014, that were obtained in the field. The observations are organized into separate appendixes according to fault trace and type of ground deformation feature, as shown in table 1.1.

Table 1.1. Index of appendixes.

Appendix number	Fault trace or ground deformation features
2	Trace A
3	Trace B
4	Trace C
5	Trace D
6	Trace E
7	Trace F
8	Trace G
9	Shaking-Induced Deformation Owing to Landslide Reactivation or Fill Settlement
10	Shaking-Related Features Resulting from Lateral Spreads and Bank Failures
11	Ridge-top fractures
12	Isolated Cracking on Slopes
13	Fractures Associated with UAVSAR Lineaments
14	Extensive Curb and Sidewalk Damage
15	Pavement Cracks South of the Soda Creek Fault

Map Explanation and Symbology

Station locations in the appendix maps are shown as circles and labeled by the Station ID number. To aid in locating a specific observation station, IDs generally increase numerically from south to north on each map. Where multiple observations occur at the exact same locality, IDs are shown as a range (for example, 200–202 identifies stations 200, 201, and 202 all at the same location). Where stations are too closely spaced to be individually labeled in the figures, a single label is used for a group of stations, with the IDs or groups of IDs listed in a vertical column and the label leader pointing to the approximate midpoint of the group of closely spaced stations.

Mappable fault rupture and surface deformation features are symbolized on the maps based on Type and Origin attributes recorded in the Rupture Esri line shape file and KML file published in the companion data release (Ponti and others, 2019) and defined in Table 4 of the main report. Fault rupture and ground deformation features are symbolized on the maps as follows:

- **Fault Rupture, well expressed** (solid black line)—rupture of inferred tectonic origin, (Origin=Tectonic) that is sufficiently continuous and has sufficiently large displacement that the rupture can be readily mapped in the field (Type=Field), observed in aerial photography (Type=Imagery), or discernible in shaded relief models derived from airborne lidar data (Type=Lidar mole track or Lidar lineament).
- **Fault Rupture mapped from InSAR data** (dashed black line)—rupture of inferred tectonic origin (Origin=Tectonic) that is not visible in airborne imagery or lidar data, but can be seen as lineaments on InSAR interferograms (Type=InSAR). In the field, fault rupture is typically observed discontinuously along strike, often only in pavement or other hardscape, with displacements that are typically small (<10 cm) and (or) distributed across zones of 5 m or more in width.
- **Fault Rupture, poorly expressed** (dash-dot black line)—rupture of presumed tectonic origin (Origin=Tectonic) inferred from InSAR data but where location and (or) continuity of rupture is uncertain owing to low correlation in the interferogram (Type=InSAR (low correlation)).
- **Fault Rupture, inferred** (dotted black line)—probable fault rupture (Origin=Tectonic) inferred to occur between observation stations (Type=Inferred) or between mapped portions of fault traces (as above), but where rupture is not otherwise observed because of very small surface displacements, incoherence/decorrelation in the InSAR data, or subaqueous rupture.
- **Ground deformation of uncertain origin** (solid purple line)—ground cracks mappable in the field (Type=Field) or from aerial photography (Type=Imagery), but where the ground deformation is interpreted to be of uncertain origin (Origin=Uncertain). Mapped fractures classified as uncertain in origin typically lack measurable displacement or a consistent sense of displacement along strike and are often seen only in pavement or compacted substrate, but neither can they be readily explained as resulting from commonly recognized earthquake-induced ground failure mechanisms such as liquefaction or shallow slope failure. Ground deformation classified as uncertain in origin may in fact be due to tectonic faulting, with surface displacements too small and (or) too broadly distributed to be readily discernible in the field. Some of these features may also be the result of secondary tectonic origin in response to rotation, folding, or distributed

shear or could result from ground shaking in the form of differential subsidence owing to variable subsurface materials, pavement decoupling, or from deep-seated, structurally-controlled gravity-driven failures (for example, block glides or ridge-spread phenomena).

- **Linear zones of ground deformation of uncertain origin, mapped from InSAR data** (dashed purple line)—zones of deformation observable as lineaments on InSAR interferograms (Type=InSAR), but where the origin of such deformation is uncertain (Origin=Uncertain), based on observations in the field.
- **Linear zones of ground deformation of uncertain origin, poorly expressed** (dash-dot purple line)—zones of ground deformation of uncertain origin (Origin=Uncertain) inferred from InSAR data but where location and (or) continuity of deformation is uncertain owing to low correlation in the interferogram (correlation coefficient <0.4; Type=InSAR (low correlation)).
- **Inferred linear zones of ground deformation of uncertain origin** (dotted purple line)—inferred linear zones of ground deformation between observation stations (Type=Inferred), where the origin of such deformation is uncertain (Origin=Uncertain).
- **Shaking-related ground deformation** (solid blue line)—linear cracks and areas mapped in the field (Type=Field) or observed in aerial photography (Type=Imagery) where the deformation is inferred to have been produced solely by shaking-induced liquefaction (lateral spreads) or shallow slope failure such as slumps, soil falls, and bank failures (Origin=Shaking).
- **Probable shaking-related ground deformation, poorly expressed** (dashed blue line)—zones of ground deformation inferred from InSAR data but where location and (or) continuity of deformation is uncertain owing to low correlation in the interferogram (correlation coefficient <0.4; Type=InSAR (low correlation)) and located within areas of previously mapped landslides.

Observation Table Explanation

Observations and (or) photographs collected at each station are tabulated by Station ID. Where stations occur at the same locality, earlier observations are listed first. Station attributes and their definitions are as follows:

- **Station ID**—identifier for the observation station. An observation station is assigned where descriptions, displacement measurements, and (or) photographs have been obtained at a location of observed fault rupture or ground deformation, on a given date and time by an observer or group of observers working together. Repeat observations at different times by the same observer or group of observers are assigned to different station IDs at the same locality.
- **Observer**—Last name of the contributor or contributors who provided the information/photographs. Full names and affiliations are listed on the report title page. In some cases, a single name is listed where observations may have been collected by a group of individuals working together.
- **Observation Date—**Date of the observation as year, numerical month, and day of month, each separated by colon (for example, 2014:09:03 represents September 3, 2014).
- **Latitude/Longitude—**Coordinate location of the observation station in decimal degrees north and west, WGS84 datum. Station coordinates are placed at the location best

interpreted as representing the location of the feature(s) being described as determined by the compilers from aerial imagery and ground photographs, or at the coordinate provided by the observer, whichever is most appropriate. We typically relocated observations of fault features to coincide with mapped fault locations as derived from high-resolution imagery, lidar data, or InSAR data. Original coordinates provided by the observer for the station location are preserved as attributes in tables within the companion data release (Ponti and others, 2019) but are not shown in the appendixes.

- **Offset Feature—**The type of feature where fault offset is observed or the type of materials that are offset or disturbed. Based on field descriptions, ground photographs, or imagery, the following classifications are used:
    - **Curb/Sidewalk—**Offset or damage to sidewalks and curbs located adjacent to roadways and typically constructed of concrete, although a small number of curbs are of asphalt construction. This classification also includes concrete patios and pathways.
    - **Foundation—**Offset or disturbance noted in concrete, brick/masonry, or wood perimeter foundations of structures.
    - **Pavement—**Offset or damage to paved roadway and runway surfaces, dominantly of asphalt construction with some concrete. Includes gravel shoulders adjacent to paved roadways,
    - **Soil—**Offset or fractures in natural ground and shallow fill. Includes compacted soil (such as dirt roads or trails) and gravel or mixed gravel/dirt roadways,
    - **Vineyard Row—**Offset noted along a row or rows of grape vines and (or) stakes,
    - **Wall/Fence—**Offset or disturbance noted in a vertical wall or fence constructed of wood, concrete, or masonry
    - **Other—**Miscellaneous feature not otherwise classified. Includes features such as decking, swimming pool shells, and railroad rails and ties.
- **Inferred Origin—**Interpreted cause of the ground deformation, either inferred directly from the observation or from context based on fracture orientation, displacement sense, setting, or nearby observations. The following classifications are used:
    - **Lateral spread—**surface cracks inferred to have been produced by lateral movement of a soil mass toward a free face, likely due to shaking-induced liquefaction or shear failure of subsurface materials.
    - **Shaking—**surface deformation inferred to have been produced solely by shaking-induced subsidence or slope failure (for example, slumps, soil falls, bank failures).
    - **Tectonic—**surface deformation observed along a linear trend, generally displaying right-lateral strike-slip displacement consistent with the earthquake source mechanism. Right-lateral offsets may be observed directly, inferred from a pattern of left-stepping en echelon surface fractures over zones several meters wide, or inferred from context based on nearby observations along the same trend. Tectonic surface rupture can include both seismogenic rupture that has propagated to the surface from the earthquake source as well as slip resulting from shallow strain release triggered by shaking or changes in near-surface stresses from the earthquake (triggered slip).
    - **Uncertain—**Surface deformation where fracture trends and observed displacements are not consistent with right-lateral fault rupture consistent with

tectonic faulting. Ground deformation of uncertain origin that is associated with InSAR lineaments may be of tectonic origin, with the lack of clear tectonic expression in the field possibly due to small fault displacements, perhaps overprinted by shaking-related settlement or pavement decoupling, or to shallow, secondary faulting that results from folding, distributed shearing and block rotations along these trends. Alternatively, these deformation zones may reflect movement along stratigraphic or structural boundaries controlling deep-seated gravity failures (for example, block glides and ridge-spread phenomena) or that separate different geologic materials that have subsided differentially owing to shaking. Sites of surface deformation not associated with linear trends and that cannot otherwise be easily explained by common earthquake-induced ground failure mechanisms (for example, liquefaction or shallow slope failure) are also included in this classification.

- **Description—**Notes and descriptive information provided by the observer, if applicable. Descriptions are edited to correct typographical and grammatical errors, and to remove irrelevant or personal information, such as property owner names, addresses, and so on. Occasionally, notes by the compilers are included.
- **Fault Azimuth—**If reported by the observer, strike of the fault zone in degrees from true north (0–360). If qualified by a double asterisk (**), the fault azimuth is estimated by the compilers in order to compute the strike-slip component of fault displacement.
- **Strike-slip**—If reported without qualification, this is the horizontal component of fault slip (in centimeters) that is resolved onto the fault plane (strike-slip displacement) as determined from direct measurement or computed from combinations of slip-vector length and orientation, fault azimuth, and horizontal displacement measurements. If qualified by an asterisk (*) the value is reported as an estimate of strike-slip displacement or represents measured horizontal offset across the fault where either the orientation of the offset azimuth, or the fault, or both, are unreported and therefore the strike-slip component cannot be confidently computed. If qualified by a double asterisk (**), strike-slip component is computed using an estimate by the compilers of the fault azimuth at the site.
- **Strike-slip Sense**—sense of strike-slip displacement, either reported, inferred from the rupture pattern, or computed from slip-vector information and fault azimuth. RL, right-lateral displacement; LL, left-lateral displacement.
- **Extension—**This is the amount of horizontal opening (extension) measured normal to the fault plane (in centimeters). It is either reported directly or computed from reported slip-vector orientation data and fault azimuth. If qualified by an asterisk (*), the reported value is an estimate. If qualified by a double asterisk (**), extension is computed using an estimate by the compilers of the fault azimuth.
- **Compression—**This is the amount of horizontal shortening (compression) measured normal to the fault plane (in centimeters), either as reported or as computed for extension. If qualified by an asterisk (*), the value is an estimate.
- **Vertical—**This is the vertical component of dip-slip displacement (in centimeters), as reported directly or computed from slip vector orientation data. If qualified by an asterisk (*), the reported value is an estimate.
- **Upthrown Side—**If a vertical component of fault displacement is reported, this is the cardinal direction of the upthrown side. N, north side up; E, east side up; S, south side up;

W, west side up. A value of "not reported" is used if vertical offset is recorded without reporting the relative sense of vertical motion.

Photographs taken at the observation station, if any, follow the station attribute information; a high-resolution image can be downloaded by clicking on the associated link. The following photograph metadata are provided in the appendixes; additional photograph metadata are published in the companion data release (Ponti and others, 2019) and defined in table 2 of the main report.

- **Photographer**—Last name of the individual who took the photograph. Full names and affiliations are listed on the title page.
- **Camera Coordinates—**Latitude (N) and longitude (W) (WGS84) of the camera GPS coordinates in decimal degrees, if available. This information is extracted from the EXIF metadata embedded within the original image file or inserted into the image file by the compilers using a corresponding GPS track log.
- **Photograph Date—**Date and time the image was taken, extracted from the EXIF metadata embedded within the original image file. Date is given as numerical year, month, and day, separated by colons, followed by a space and then followed by hours, minutes, and seconds, also separated by colons (for example, 2014:08:24 11:45:19 represents August 24, 2014, 11:45:19 AM). Time of day is given in 24-hour notation (military time), Pacific Daylight Time (GMT-7).

Manuscript approved on February 25, 2019

For more information about this publication, contact
Director
Earthquake Science Center
U.S. Geological Survey
345 Middlefield Road, Mail Stop 977
Menlo Park, CA 94025

Publishing support provided by the
Menlo Park Publishing Service Center